# Improved CRB for Millimeter-Wave Radar with 1-bit ADCs

Khurram Usman Mazher<sup>®</sup>, *Student Member, IEEE*, Amine Mezghani<sup>®</sup>, *Member, IEEE*, and Robert W. Heath Jr.<sup>®</sup>, *Fellow, IEEE* 

Millimeter-wave is widely used for consumer radar applications like driver assistance systems in automated vehicles and gesture recognition in touch-free interfaces. To cope with the increased hardware complexity, higher costs and power consumption of wideband systems at millimeter-wave frequencies, we propose a fully digital architecture with low-resolution analog-to-digital converters (ADCs) on each radio-frequency chain. The effect of the low-resolution ADCs on radar parameter estimation is characterized by the Cramér-Rao bound (CRB) under the proposed hardware constraints. Prior work has shown that at low signal-to-noise ratio, a radar system with 1-bit ADCs suffers a performance loss of 2dB in parameter estimation compared to a system with ideal infinite resolution ADCs. In this paper, we design an analog preprocessing unit that beamforms in a particular direction and improves the system performance in terms of the achievable CRB. We optimize the proposed preprocessing architecture and show that the optimized network is realizable through low-cost low-resolution phase-shifters. With the optimized preprocessor network in the system, we reduce the gap to 1.16dB compared to a system with ideal ADCs. We demonstrate the potential of the proposed architecture to meet the requirements of high-resolution sensing through analytical derivation and numerical computation of an improved CRB and show its achievability through a correlation-based estimator.

Index Terms—1-bit ADC, Analog preprocessing, Bussgang decomposition, Cramér-Rao bound, Fisher information, Radar

### I. INTRODUCTION

The larger bandwidths available at millimeter-wave (mmWave) frequencies have the potential to enable high data rate communications and high-resolution sensing. The communication data rate and the radar resolution improve linearly with the signal bandwidth [1]. The excessive power consumption and increased cost of high-resolution ADCs at these larger bandwidths is a limiting factor [2]. In addition, the implementation of power amplifiers and low noise amplifiers on a radio-frequency (RF) chain behind each antenna element is practically prohibitive at mmWave frequencies. To enable practical implementation, we propose a new radar architecture with 1-bit ADCs while maintaining a separate RF chain perantenna. In addition to driving the cost and power consumption low, 1-bit ADCs reduce complexity at the RF level, making the fully digital architecture a viable option for further research.

There is limited work on low-resolution ADCs for mmWave radar. Compressive sensing based solutions for a single-input single-output (SISO) 1-bit radar have been proposed [3], [4]. The results, however, were limited only to numerical examples with no theoretical comparison in terms of the mean squared error (MSE). Similarly, a maximum a posteriori (MAP) approach applied to 1-bit radar has been demonstrated through examples [5]. A low-rank matrix recovery problem based solution for 1-bit radar parameter estimation was numerically evaluated in [6]. The lack of a theoretical performance benchmark, against which the different proposed algorithms

Manuscript received on December 31, 2020. This work was supported by a gift from Qualcomm Inc.

for 1-bit ADC radar can be evaluated, motivates our study of the effect of 1-bit ADCs on the radar parameter estimation performance.

Low signal-to-noise ratio (SNR) reduction of channel capacity by a factor of  $2/\pi$  ( $\approx$  2dB) in 1-bit constrained communication systems is a well-studied problem [7]. The loss in SISO channel capacity in an additive white Gaussian noise (AWGN) setting at low SNR due to 1-bit quantization may be reduced by asymmetric quantization and oversampling [8], [9]. A similar reduction in channel capacity loss for 1-bit systems at low SNRs was also observed under a correlated noise model based on a Toeplitz noise covariance matrix [10]. This line of research has also gathered interest in recent years. The 2dB loss in channel phase estimation was shown to be reduced to 0.9dB by 6× oversampling [11]. The CRB of channel parameter estimation for a 1-bit system was improved by oversampling the received signal for three different types of channel models [12]. Similar observations have also been made in the context of positioning and navigation systems. Optimization of the antialiasing filter bandwidth and oversampling factor was shown to reduce the root mean squared error (RMSE) in delay estimation for a 1-bit GPS system from 2dB to 1dB [13], with the biggest improvements coming from oversampling. Similarly, time of flight and attenuation gain estimation errors were shown to surpass the 2dB limit by oversampling the received signal [14]. Similar improvements for a general signal model were demonstrated by oversampling and antialiasing filter optimization [15]. The common observation across [7]–[15] is that oversampling and antialiasing filter optimization, both of which make the noise correlated, improve the performance of 1-bit systems. Nonetheless, this ability incurs a computational, power and memory cost in addition to higher cost of ADCs capable of  $\approx 10 \times$  oversampling.

Inspired by the improvements observed under a correlated noise model in 1-bit ADC based systems, we introduce another dimension to optimize the design process for 1-bit

1

K. U. Mazher (khurram.usman@utexas.edu) is with the Wireless Networking and Communications Group, The University of Texas at Austin, Austin, TX 78712 USA.

A. Mezghani (amine.mezghani@umanitoba.ca) is with the Electrical and Computer Engineering department at the University of Manitoba, Winnipeg, MB R3T 2N2, Canada.

R. W. Heath Jr. (rwheathjr@ncsu.edu) is with the Electrical and Computer Engineering department at the North Carolina State University, Raleigh, NC 27695 USA.

radar systems. The proposed modification is also applicable to positioning/navigation and communication systems. We propose a simple analog preprocessor that is introduced in each RF chain before quantization and derive the CRB for the 1-bit radar parameter estimation problem with the proposed analog preprocessor based on the Bussgang decomposition [16]. The proposed analog preprocessor, which is a  $[1 \quad \alpha]^T$ spatial filter, beamforms in a particular direction and makes the noise correlated across consecutive RF chains. The main result of the paper is the improvement in the 2dB loss due to 1-bit quantization through the introduction of the proposed preprocessor. We evaluate this improvement in terms of the CRB and compare the proposed architecture with and without the analog preprocessor present in the system, and also to the ideal ADCs with  $\infty$  resolution. Our results suggest that the proposed architecture is an appropriate low-cost low-power radar solution capable of meeting the high-resolution sensing requirements. The main contributions of this paper can be summarized as:

- We derive the CRB for a fully digital radar architecture with 1-bit ADCs on each RF chain and demonstrate its tightness to a lower bound on Fisher information introduced in prior work [17].
- We propose an analog preprocessing unit that can improve upon the 2dB loss due to 1-bit quantization at low SNRs known in prior work [7]. Due to the intractability of the CRB with the analog preprocessing unit and the tightness of the lower bound established earlier, we derive the CRB for the analog preprocessing architecture using the lower bound in [17]. This results in a 0.84dB improvement over the case without the proposed analog preprocessor.
- We optimize the analog preprocessing unit (depending on the application) over the design parameter α based on the improved CRB. Of note, the optimized preprocessing unit is realizable through low-resolution phase-shifters. Moreover, we show that the optimized preprocessing can get to within 1.16dB of ideal ∞-resolution ADCs.
- Our numerical evaluation of the CRB agrees with the derived analytical results and demonstrates an improvement over the prior known results. We also show that the improved CRB can be achieved using a correlationbased range and direction of arrival (DoA) estimator and provide future directions for generalization of this work.

In our prior work [18], we explored the tradeoffs between the communication and sensing requirements of a joint communication radar (JCR) system using the same architecture (without the preprocessor) as in this paper [19]. We concluded that the proposed architecture is a potential solution for joint high rate communication and high-resolution sensing and suffers a 2dB loss in terms of channel capacity for communication and parameter estimation error for radar at low SNRs. In [20], we published initial results from the detailed study carried out in this paper for a *fixed* spatial beamformer [1 1]<sup>T</sup>. Our new work, however, is a significant extension of [18], [20]. In addition to deriving the exact CRB for the 1-bit system and showing its tightness to the lower bound to Fisher information

used in [18] and [20], we generalize the analog preprocessor to a  $[1 \ \alpha]^T$  spatial filter. We then optimize the more general preprocessing network to achieve maximum improvement in terms of the CRB and show that the optimized preprocessor can be implemented using low-resolution phase-shifters. Last but not the least, the achievability of the improved CRB demonstrated in this paper is another aspect missing from our previous work [20].

The rest of this paper is organized as follows. In Section III, we describe the system model. In Section III, we derive the CRB for the 1-bit architecture, introduce a lower bound to Fisher information and demonstrate its tightness under white noise to the analytical bound. Next in Section IV, we introduce the analog preprocessing unit which is a main contribution of this paper. In Section V, we derive the CRB for the proposed architecture with the analog preprocessing unit. The preprocessing unit is optimized in Section VI. The CRB results and its achievability are presented in Section VII before concluding the paper with potential directions for future work in Section VIII.

Notation:  $\mathbf{B}$  is a matrix,  $\mathbf{b}$  is a vector and b is a scalar.  $\mathbf{B}_i$  and  $\mathbf{B}_{ij}$  denotes the  $i^{th}$  row and  $i^{th}, j^{th}$  entry of the matrix **B**.  $\mathbf{b}_i$  denote the  $i^{th}$  entry of **b**. The operator  $(\cdot)^T$ and  $(\cdot)^*$  denote the transpose and conjugate transpose of a matrix/vector.  $\overline{\mathbf{b}}$  represents the fast Fourier transform (FFT) of b. diag(B) denotes a diagonal matrix containing only the diagonal elements of B. diag(b) denotes a diagonal matrix with the elements of b on the main diagonal. The function sgn(a) denotes the signum function applied component-wise to the Re(a) (real) and Im(a) (imaginary) parts of a complex number a. The operator  $\odot$  denotes the Hadamard product of two vectors/matrices.  $||\mathbf{b}||_p$  is the p-norm of b. The notations  $|\cdot|, (\cdot)^k$  and  $\angle(\cdot)$  denote the absolute value,  $k^{th}$  power and phase operation applied to a scalar or element-wise to a vector/matrix. The matrix  $I_N$  denotes an identity matrix of size  $N \times N$ .  $\mathbf{F}_N$  is the FFT matrix of size  $N \times N$  normalized by  $\frac{1}{\sqrt{N}}$ .  $\mathbf{e}_i$  is the N-dimensional canonical basis vector with 1 at the  $i^{th}$  position and zeros elsewhere.  $\mathcal{N}(\mu, \Sigma)$  denotes a complex Gaussian multi-variate distribution with mean  $\mu$ and covariance  $\Sigma$ .  $Q(\cdot)$  denotes the cumulative tail probability of a standard normal random variable as a function of its argument  $(\cdot)$ . c is the speed of light. The sinc pulse is defined as  $\operatorname{sinc}(x) = \frac{\sin(\pi x)}{\pi x}$ . The notations  $|\mathcal{S}|$  denotes the cardinality of the set  $\mathcal{S}$ .  $\mathbf{A} \succeq \mathbf{B}$  denotes the matrix property of positive semi-definiteness given by  $\mathbf{x}^{T}(\mathbf{A} - \mathbf{B})\mathbf{x} > 0 \,\forall \, \mathbf{x} \in \mathcal{R}^{N}$ .

#### II. SYSTEM MODEL

Consider a radar system with co-located transmit (TX) and receive (RX) antennas as shown in Fig. 1. The TX is equipped with an  $N_{\rm TX}$  element antenna array that operates in an analog beamforming manner and beamforms at  $\theta_{\rm BF}$ . The beamforming angle  $\theta_{\rm BF}$  depends on the application. The RX is equipped with a fully digital uniform linear array (ULA) of  $N_{\rm RX}$  elements with an inter-element spacing of  $d=\frac{\lambda}{2}$ , where  $\lambda$  is the carrier frequency wavelength. Fully digital radar architectures are becoming more common with the development of multiple-input multiple-output (MIMO)

radar [21]–[23]. While the presented results are for the ULA geometry, however, the proposed methodology can easily be extended to other array types such as uniform planar arrays by making the appropriate changes to the proposed analog preprocessor in Section IV. The presented analysis can be similarly extended by accounting for the additional dimension. The TX and RX arrays are closely separated by a distance of  $d_{\rm si}$  m such that they see the same target location parameters while providing adequate isolation for full-duplex operation. Further, the TX array is assumed to have a reduced gain in the end-fire ( $\theta=\pm90^{\circ}$ ) direction thus providing suppression of self-interference. The residual self-interference from the TX to the RX is incorporated into our signal model. We later note that the proposed analog preprocessor reduces the constraints on the TX antenna beam-pattern design.

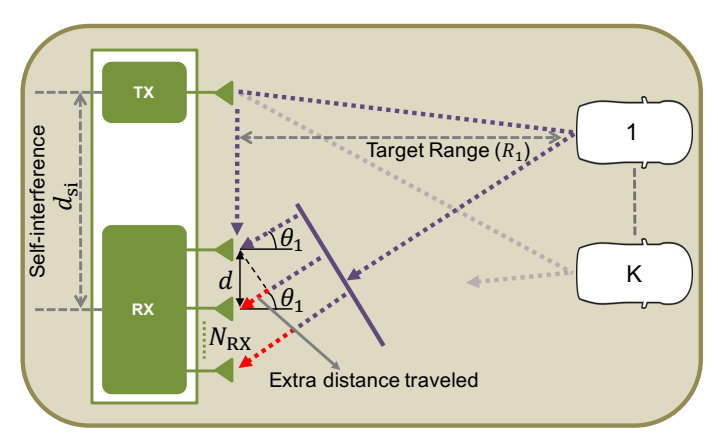


Fig. 1: The channel model with self-interference due to colocated TX and RX antennas and reflection from K targets. The TX array operates in analog beamforming mode (hence shown as a single antenna). The RX array with  $N_{\rm RX}$  elements operates in a fully digital beamforming mode. The extra distance traveled by the planar wave between the antenna elements (shown in red) is modeled by the RX array response vector under the narrowband assumption.

Self-interference due to co-located TX and RX antennas and the reflection from the K targets result in the (K+1)-path channel model shown in Fig. 1. Assuming there is no blockage between the TX and the targets, the RX receives a delayed and attenuated copy of the transmitted signal after reflection from the target along with residual self-interference. The selfinterference path is characterized by its complex channel gain  $\gamma_0$ , its delay  $\tau_0=\frac{d_{\rm si}}{c}$ , and its DoA  $\theta_0=-90^\circ$ . Similarly, the path reflected off of the  $k^{th}$  target is characterized by its complex channel gain  $\gamma_k$ , its delay  $\tau_k = \frac{2R_k}{c}$ , where  $R_k$  is the distance of the  $k^{th}$  target from the TX/RX and its DoA  $\theta_k$ . The end-to-end complex channel gains  $\{\gamma_0, \gamma_1 \dots \gamma_K\}$  include the contribution of the TX/RX antenna gains, transmit power  $P_t$  and distance-dependent path-loss. Additionally, the channel coefficients corresponding to target reflections,  $\{\gamma_1 \dots \gamma_K\}$ , incorporate the effect of the radar cross-section (RCS) area  $\zeta_k$  of each target as well. In this work, the radar targets are assumed to be of Swerling type 0, each target with its own constant RCS area  $\zeta_k$  [1, Ch. 6]. The CRB is evaluated given that the parameters are unknown but deterministic and hence deterministic Swerling type 0 targets with no variations are a good assumption here. For ease of exposition, we only consider stationary targets in this paper and are thus limited to the 2D range-DoA parameter space. The presented analysis can be extended to include Doppler, with similar gains expected for the Doppler dimension as for the range and DoA dimensions.

#### A. Transmit signal model

Consider a coherent processing interval (CPI) of T seconds in which L known independent and identically distributed (IID) symbols  $s[\ell]$ , drawn from a zero mean circularly symmetric unit variance complex Gaussian distribution (i.e.  $\mathbb{E}[|s[\ell]|^2] = 1$ ), are transmitted after being filtered through the unit energy pulse shape g(t) with symbol period  $T_s$ . The complex baseband signal at the TX is given by

$$x(t) = \sqrt{P_t} \sum_{\ell=1}^{L} s[\ell]g(t - \ell T_s). \tag{1}$$

We use the *sinc* pulse filter in this paper with  $g(t) = \operatorname{sinc}(Bt)$ . The bandwidth B of the pulse shaping filter is related to its symbol period  $T_s$  as  $B = \frac{1}{T_s}$ . We note here that the given transmit signal model is well suited for both radar and communication. In addition, the results that follow can be generalized to other pulse shaping filters such as root raised cosine and other radar waveforms such as orthogonal frequency division multiplexing and frequency modulated continuous waveform.

# B. Receive signal model

Under the narrowband assumption, the extra distance between the RX antenna elements (shown in red in Fig. 1) traveled by a planar wave incident from a far-field source can be modeled by the direction-dependent linear phase change array response vector  $\mathbf{a}(\theta) \in \mathcal{C}^{N_{\mathrm{RX}} \times 1}$  given by  $[1 \ e^{\frac{\mathrm{j} 2\pi d \sin(\theta)}{\lambda}} \ e^{\frac{\mathrm{j} 4\pi d \sin(\theta)}{\lambda}} \ \dots \ e^{\frac{\mathrm{j} (N_{\mathrm{RX}}-1)2\pi d \sin(\theta)}{\lambda}}]^{\mathrm{T}}$ . Let  $\tau_{\mathrm{max}}$  denote the time of flight of the maximum feasible target determined by the link budget or by the duty cycle of the radar and  $\mathbf{n}(t)$  the noise vector the elements of are assumed to be IID over a zero-mean circularly symmetric complex Gaussian distribution with covariance matrix  $\sigma^2\mathbf{I}_N$ . With these definitions, the signal received at the RX array for  $0 \leq t \leq (T + \tau_{\mathrm{max}})$  can be written as

$$\mathbf{y}(t) = \underbrace{\sum_{k=0}^{K} \gamma_k \mathbf{a}(\theta_k) x(t - \tau_k)}_{\mathbf{s}(t; \boldsymbol{\psi})} + \mathbf{n}(t). \tag{2}$$

The signal part of the observation,  $\mathbf{s}(t; \boldsymbol{\psi})$ , depends on the deterministic yet unknown parameter vector  $\boldsymbol{\psi} = \{|\gamma_0|, \angle\gamma_0, \theta_0, \tau_0, |\gamma_1| \dots \tau_K\}$ . The signal after sampling at the Nyquist rate and 1-bit quantization is given by

$$\mathbf{q}[n] = \operatorname{sgn}(\mathbf{y}(nT_s)) = \underbrace{\operatorname{sgn}(\operatorname{Re}\left[\mathbf{y}(nT_s)\right])}_{\mathbf{u}[n]} + \operatorname{j}\underbrace{\operatorname{sgn}(\operatorname{Im}\left[\mathbf{y}(nT_s)\right])}_{\mathbf{v}[n]}, \quad (3)$$

for  $n \in \mathcal{T} = \{0 \dots N\}$ . Here  $N = \lceil \frac{T + \tau_{\max}}{T_s} \rceil$  denotes the number of samples captured at the RX during one CPI. From this point onwards, we do not explicitly write the time index for ease of exposition. All the derived formulas and bounds are for a single time sample and capturing multiple time samples leads to an accumulating effect because of the additivity of Fisher information as a result of independence across time samples [24]. The RX signal model with analog preprocessing will be described in Section IV.

### III. CRAMÉR-RAO BOUND

The CRB is a lower bound on the estimation error performance of any unbiased estimator [24, Ch. 3]. The CRB of the  $i^{th}$  element of a parameter vector  $\boldsymbol{\psi}$ ,  $[\text{CRB}(\boldsymbol{\psi})]_i$ , is given by the inverse of the Fisher information matrix (FIM)  $\mathbf{F}(\boldsymbol{\psi})$  as  $[\text{CRB}(\boldsymbol{\psi})]_i = [\mathbf{F}^{-1}(\boldsymbol{\psi})]_{i,i}$  [24]. Fisher information is a measure of the amount of information conveyed by the observed samples about the parameters to be estimated. The  $i^{th}$ ,  $j^{th}$  entry of the FIM for the output  $\mathbf{r}(t;\boldsymbol{\psi})$  of a multivariate system that depends on the unknown deterministic parameters  $\boldsymbol{\psi}$  through the likelihood function  $p(\mathbf{r}|\mathbf{s}(\boldsymbol{\psi}))$  is given by [24]

$$[\mathbf{F}_{\mathbf{r}}(\boldsymbol{\psi})]_{ij} = \mathbb{E}_{p(\mathbf{r}|\mathbf{s}(\boldsymbol{\psi}))} \left[ \left( \frac{\partial \ln p(\mathbf{r}|\mathbf{s}(\boldsymbol{\psi}))}{\partial \boldsymbol{\psi}_i} \right)^{\mathrm{T}} \times \left( \frac{\partial \ln p(\mathbf{r}|\mathbf{s}(\boldsymbol{\psi}))}{\partial \boldsymbol{\psi}_i} \right) \right]. \tag{4}$$

We first derive the exact CRB for the radar parameters  $\psi$  under 1-bit quantization using (4). We then discuss a lower bound to the Fisher information measure [17] and demonstrate its tightness to the exact CRB based on the Bussgang decomposition [16] for the system with 1-bit quantization. This lower bound is then used to derive the CRB for the system with the proposed analog preprocessor in Section V.

### A. Exact radar parameter CRB under1-bit quantization

For the signal model in (3), the likelihood function  $p(\mathbf{q}|\mathbf{s}(\psi))$  takes the product form because  $\mathbf{q}_i$  and  $\mathbf{q}_j$  for  $i \neq j$  are conditionally independent given  $\mathbf{s}(\psi)$ . The likelihood function  $p(\mathbf{q}|\mathbf{s}(\psi))$  is given by

$$p(\mathbf{q}|\mathbf{s}(\boldsymbol{\psi})) = \prod_{k=1}^{N_{\text{RX}}} p(\mathbf{q}_k|\mathbf{s}_k(\boldsymbol{\psi}))$$

$$= \prod_{k=1}^{N_{\text{RX}}} p(\mathbf{u}_k|\mathbf{s}_k(\boldsymbol{\psi})) p(\mathbf{v}_k|\mathbf{s}_k(\boldsymbol{\psi})).$$
(5)

The positive orthant probability for  $\mathbf{u}_k$  is given by

$$p(\mathbf{u}_{k} = +1|\mathbf{s}_{k}(\boldsymbol{\psi})) = \frac{1}{\sqrt{\pi}\sigma} \int_{-\operatorname{Re}[\mathbf{s}_{k}(\boldsymbol{\psi})]}^{\infty} \exp\left(-\frac{x^{2}}{\sigma^{2}}\right) dx$$
$$= Q\left(-\frac{\operatorname{Re}[\mathbf{s}_{k}(\boldsymbol{\psi})]}{\sigma/\sqrt{2}}\right).$$
(6)

The corresponding negative orthant probability can be written

$$p(\mathbf{u}_{k} = -1|\mathbf{s}_{k}(\boldsymbol{\psi})) = \frac{1}{\sqrt{\pi}\sigma} \int_{-\infty}^{-\operatorname{Re}[\mathbf{s}_{k}(\boldsymbol{\psi})]} \exp\left(-\frac{x^{2}}{\sigma^{2}}\right) dx$$
$$= Q\left(\frac{\operatorname{Re}[\mathbf{s}_{k}(\boldsymbol{\psi})]}{\sigma/\sqrt{2}}\right). \tag{7}$$

For  $\mathbf{u}_k \in \{+1, -1\}$ , (6) and (7) can be combined to compactly write  $p(\mathbf{u}_k | \mathbf{s}_k(\boldsymbol{\psi}))$  as

$$p(\mathbf{u}_k|\mathbf{s}_k(\boldsymbol{\psi})) = Q\left(-\frac{\mathbf{u}_k \operatorname{Re}\left[\mathbf{s}_k(\boldsymbol{\psi})\right]}{\sigma/\sqrt{2}}\right). \tag{8}$$

Similarly for  $\mathbf{v}_k \in \{+1, -1\}$ , the probability  $p(\mathbf{v}_k | \mathbf{s}_k(\boldsymbol{\psi}))$  is given by

$$p(\mathbf{v}_k|\mathbf{s}_k(\boldsymbol{\psi})) = Q\left(-\frac{\mathbf{v}_k \text{Im}\left[\mathbf{s}_k(\boldsymbol{\psi})\right]}{\sigma/\sqrt{2}}\right). \tag{9}$$

Using (5), (8) and (9), the log-likelihood  $\ln(p(\mathbf{q}|\mathbf{s}(\psi)))$  of the 1-bit quantized observation vector  $\mathbf{q}$  can be written as

$$\ln(p(\mathbf{q}|\mathbf{s}(\boldsymbol{\psi}))) = \sum_{k=1}^{N_{\text{RX}}} \ln\left(Q\left(-\frac{\mathbf{u}_k \text{Re}\left[\mathbf{s}_k(\boldsymbol{\psi})\right]}{\sigma/\sqrt{2}}\right)\right) + \ln\left(Q\left(-\frac{\mathbf{v}_k \text{Im}\left[\mathbf{s}_k(\boldsymbol{\psi})\right]}{\sigma/\sqrt{2}}\right)\right).$$
(10)

The contribution to the FIM  $\mathbf{F_q}(\psi)$  from the real and imaginary parts of the observation vector  $\mathbf{q}$  can be split into two parts,  $\mathbf{F_u}(\psi)$  and  $\mathbf{F_v}(\psi)$ , because of the independence of  $\mathbf{u}$  and  $\mathbf{v}$  conditioned on  $\mathbf{s}(\psi)$  as [25]

$$\mathbf{F}_{\mathbf{q}}(\boldsymbol{\psi}) = \mathbf{F}_{\mathbf{q}}(\boldsymbol{\psi}) + \mathbf{F}_{\mathbf{v}}(\boldsymbol{\psi}). \tag{11}$$

From here onwards we restrict our attention towards deriving  $\mathbf{F_u}(\psi)$ , the FIM for Re [q], while keeping in mind that  $\mathbf{F_v}(\psi)$  can be derived in an analogous manner. With  $\frac{\partial \ln(Q(f(\cdot)))}{\partial(\cdot)}$  taking the form

$$\frac{\partial \ln \left( Q(f(\cdot)) \right)}{\partial (\cdot)} = -\frac{\exp \left( -f^2(\cdot)/2 \right) \times \frac{\partial f(\cdot)}{\partial (\cdot)}}{\sqrt{2\pi} Q(f(\cdot))}, \quad (12)$$

the contribution of the  $k^{th}$  component of  ${\bf u}$  to the  $i^{th}, j^{th}$  entry of the FIM ,  $[{\bf F}_{{\bf u}_k}(\psi)]_{ij}$ , according to (4) is given by

$$[\mathbf{F}_{\mathbf{u}_{k}}(\boldsymbol{\psi})]_{ij} = \frac{1}{\pi\sigma^{2}} \mathbb{E}_{p(\mathbf{u}_{k}|\boldsymbol{\psi})} \left[ \frac{\exp\left(-2\operatorname{Re}\left[\mathbf{s}_{k}(\boldsymbol{\psi})\right]^{2}/\sigma^{2}\right)}{Q\left(-\sqrt{2}\mathbf{u}_{k}\operatorname{Re}\left[\mathbf{s}_{k}(\boldsymbol{\psi})\right]/\sigma\right)^{2}} \times \frac{\partial\operatorname{Re}\left[\mathbf{s}_{k}(\boldsymbol{\psi})\right]}{\partial\psi_{i}} \frac{\partial\operatorname{Re}\left[\mathbf{s}_{k}(\boldsymbol{\psi})\right]}{\partial\psi_{j}} \right].$$
(13)

The details of the derivatives  $\frac{\partial \mathrm{Re}[\mathbf{s}_k(\psi)]}{\partial \psi_i}$  and  $\frac{\partial \mathrm{Im}[\mathbf{s}_k(\psi)]}{\partial \psi_j}$  are deferred to Section III-A. Combining (6), (7) and (13)

$$[\mathbf{F}_{\mathbf{u}_{k}}(\boldsymbol{\psi})]_{ij} = \frac{1}{\pi\sigma^{2}} \frac{\partial \operatorname{Re}\left[\mathbf{s}_{k}(\boldsymbol{\psi})\right]}{\partial \boldsymbol{\psi}_{i}} \frac{\partial \operatorname{Re}\left[\mathbf{s}_{k}(\boldsymbol{\psi})\right]}{\partial \boldsymbol{\psi}_{j}} \times \frac{\exp\left(-2\operatorname{Re}\left[\mathbf{s}_{k}(\boldsymbol{\psi})\right]^{2}/\sigma^{2}\right)}{Q\left(-\sqrt{2}\operatorname{Re}\left[\mathbf{s}_{k}(\boldsymbol{\psi})\right]/\sigma\right) Q\left(\sqrt{2}\operatorname{Re}\left[\mathbf{s}_{k}(\boldsymbol{\psi})\right]/\sigma\right)}.$$
(14)

Making use of the the additivity of the real and imaginary parts in (11), the final FIM  $[\mathbf{F}_{\mathbf{q}}(\psi)]_{ij}$  can be written as

$$[\mathbf{F}_{\mathbf{q}}(\boldsymbol{\psi})]_{ij} = \frac{1}{\pi\sigma^{2}} \sum_{k=1}^{N_{\text{RX}}} \left( \frac{\partial \text{Re}\left[\mathbf{s}_{k}(\boldsymbol{\psi})\right]}{\partial \boldsymbol{\psi}_{i}} \frac{\partial \text{Re}\left[\mathbf{s}_{k}(\boldsymbol{\psi})\right]}{\partial \boldsymbol{\psi}_{j}} \times \frac{\exp\left(-2\text{Re}\left[\mathbf{s}_{k}(\boldsymbol{\psi})\right]^{2}/\sigma^{2}\right)}{Q\left(-\sqrt{2}\text{Re}\left[\mathbf{s}_{k}(\boldsymbol{\psi})\right]/\sigma\right) Q\left(\sqrt{2}\text{Re}\left[\mathbf{s}_{k}(\boldsymbol{\psi})\right]/\sigma\right)} + \frac{\partial \text{Im}\left[\mathbf{s}_{k}(\boldsymbol{\psi})\right]}{\partial \boldsymbol{\psi}_{i}} \frac{\partial \text{Im}\left[\mathbf{s}_{k}(\boldsymbol{\psi})\right]}{\partial \boldsymbol{\psi}_{j}} \times \frac{\exp\left(-2\text{Im}\left[\mathbf{s}_{k}(\boldsymbol{\psi})\right]^{2}/\sigma^{2}\right)}{Q\left(-\sqrt{2}\text{Im}\left[\mathbf{s}_{k}(\boldsymbol{\psi})\right]/\sigma\right) Q\left(\sqrt{2}\text{Im}\left[\mathbf{s}_{k}(\boldsymbol{\psi})\right]/\sigma\right)},$$
(15)

where the summation is over the  $N_{\rm RX}$  samples captured across the  $N_{\rm RX}$  RX antennas.

In the low per-antenna SNR regime  $(\sigma \gg |\mathbf{s}_k(\psi)|)$ , which is a valid assumption at mmWave frequencies, (15) can be approximated (up to first order in terms of  $\mathbf{s}_k(\psi)/\sigma$ ) as

$$[\mathbf{F}_{\mathbf{q}}(\boldsymbol{\psi})]_{ij} \approx \frac{4}{\pi\sigma^{2}} \sum_{k=1}^{N_{\text{RX}}} \left( \frac{\partial \text{Re}\left[\mathbf{s}_{k}(\boldsymbol{\psi})\right]}{\partial \boldsymbol{\psi}_{i}} \frac{\partial \text{Re}\left[\mathbf{s}_{k}(\boldsymbol{\psi})\right]}{\partial \boldsymbol{\psi}_{j}} + \frac{\partial \text{Im}\left[\mathbf{s}_{k}(\boldsymbol{\psi})\right]}{\partial \boldsymbol{\psi}_{i}} \frac{\partial \text{Im}\left[\mathbf{s}_{k}(\boldsymbol{\psi})\right]}{\partial \boldsymbol{\psi}_{j}} \right).$$
(16)

The FIM for the ideal infinite precision signal y in (2) from [1]

$$[\mathbf{F}_{\mathbf{y}}(\boldsymbol{\psi})]_{ij} = \frac{2}{\sigma^{2}} \sum_{k=1}^{N_{\mathrm{RX}}} \left( \frac{\partial \mathrm{Re}\left[\mathbf{s}_{k}(\boldsymbol{\psi})\right]}{\partial \boldsymbol{\psi}_{i}} \frac{\partial \mathrm{Re}\left[\mathbf{s}_{k}(\boldsymbol{\psi})\right]}{\partial \boldsymbol{\psi}_{j}} + \frac{\partial \mathrm{Im}\left[\mathbf{s}_{k}(\boldsymbol{\psi})\right]}{\partial \boldsymbol{\psi}_{i}} \frac{\partial \mathrm{Im}\left[\mathbf{s}_{k}(\boldsymbol{\psi})\right]}{\partial \boldsymbol{\psi}_{j}} \right).$$
(17)

Comparing (16) and (17), 1-bit sampling leads to a  $2/\pi$  loss ( $\approx$  2dB) in Fisher information at low SNR compared to infinite resolution sampling. This result has been observed before in the context of capacity loss [7] and channel estimation [11].

# B. Lower bound for Fisher information measure

The product form of the likelihood of the quantized observation vector q in (5) makes the computation of the exact FIM in (4) tractable. Under a correlated noise model (which will be the case with the proposed analog preprocessor), the computation in (4) becomes very difficult. With this foresight, we introduce an information measure that is a pessimistic approximation of the exact FIM in (4) using only the first moment  $\mu(\psi)$  and the second central moment  $\Sigma(\psi)$  of the likelihood function  $p(\mathbf{q}|\mathbf{s}(\boldsymbol{\psi}))$ . It has been shown in prior work that amongst all possible additive noise distributions with fixed variance, the Gaussian distribution minimizes the Fisher information measure and provides a conservative estimate of the performance of any system [17]. For a parametric probabilistic system  $p(\mathbf{r}|\mathbf{s}(\boldsymbol{\psi}))$  with unknown deterministic parameters  $\psi \in \Psi$  and observed system output  $\mathbf{r}(\psi)$ , the FIM  $\mathbf{F_r}(\psi)$  dominates the FIM  $\mathbf{F_{\tilde{r}}}(\psi)$  of an equivalent Gaussian system  $q(\tilde{\mathbf{r}}|\mathbf{s}(\boldsymbol{\psi}))$  with first and second central moments matched to the original system  $p(\mathbf{r}|\mathbf{s}(\boldsymbol{\psi}))$  and  $\mathbf{r}(\boldsymbol{\psi}) = \tilde{\mathbf{r}}(\boldsymbol{\psi})$  [17]. When  $\frac{\partial \Sigma(\psi)}{\partial \psi}=0$ , this equivalent pessimistic Gaussian approximation is given by

$$\mathbf{F}_{\mathbf{r}}(\psi) \succeq \mathbf{F}_{\tilde{\mathbf{r}}}(\psi) = \left(\frac{\partial \mu(\psi)}{\partial \psi}\right)^{\mathrm{T}} \mathbf{\Sigma}^{-1}(\psi) \left(\frac{\partial \mu(\psi)}{\partial \psi}\right).$$
 (18)

The lower bound in (18) was derived under the assumption of support of the random process  $\mathbf{r}(\psi)$  on real numbers [17]. In fact, (18) corresponds to the exact Fisher information of a real Gaussian process when  $\frac{\partial \Sigma(\psi)}{\partial \psi} = 0$ . Using the independence of the real and imaginary parts of the observation  $\mathbf{r}(\psi)$  under which (11) holds true, the bound (18) can be extended to complex numbers by using the Fisher information chain rule [25]. The lower bound for complex random processes is then given by the FIM of a complex Gaussian process [24]

$$\mathbf{F}_{\mathbf{r}}(\boldsymbol{\psi}) \succeq \mathbf{F}_{\tilde{\mathbf{r}}}(\boldsymbol{\psi}) = 2\text{Re}\left[\left(\frac{\partial \boldsymbol{\mu}(\boldsymbol{\psi})}{\partial \boldsymbol{\psi}}\right)^* \boldsymbol{\Sigma}^{-1}(\boldsymbol{\psi}) \left(\frac{\partial \boldsymbol{\mu}(\boldsymbol{\psi})}{\partial \boldsymbol{\psi}}\right)\right]. \tag{19}$$

In Section III-C, we use the Bussgang decomposition to demonstrate the tightness of (19) to the exact FIM in (4) at low SNRs.

#### C. Bussgang decomposition-based CRB

The *Bussgang* theorem [16] states that the output of the non-linear 1-bit ADC q in (3) can be decomposed into a desired signal component and an uncorrelated distortion e as

$$\mathbf{q} = \mathbf{D}\mathbf{y} + \mathbf{e}.\tag{20}$$

The linear transformation  $\mathbf{D}$  is obtained from the linear minimum mean squared error (LMMSE) estimate of  $\mathbf{q}$  from  $\mathbf{y}$  given by

$$\mathbf{D} = \mathbb{E}[\mathbf{q}\mathbf{y}^*]\mathbb{E}[\mathbf{y}\mathbf{y}^*]^{-1} = \mathbf{R}_{\mathbf{q}\mathbf{y}}\mathbf{R}_{\mathbf{v}\mathbf{v}}^{-1}.$$
 (21)

The correlation matrix of the uncorrelated distortion error e can then be written as

$$\mathbf{R_{ee}} = \mathbb{E}[(\mathbf{q} - \mathbf{Dy})(\mathbf{q} - \mathbf{Dy})^*] = \mathbf{R_{qq}} - \mathbf{R_{qy}} \mathbf{R_{yy}^{-1}} \mathbf{R_{yq}}.$$
(22)

Based on this decomposition, the quantized observation vector  $\mathbf{q}[n]$  in (3) can be written as

$$\mathbf{q}[n] = \mathbf{D}\mathbf{y}[n] + \mathbf{e}[n]$$

$$= \mathbf{D}\sum_{k=0}^{K} \gamma_k \mathbf{a}(\theta_k) x(nT_s - \tau_k) + \mathbf{D}\mathbf{n}[n] + \mathbf{e}[n]$$

$$= \mathbf{D}\sum_{k=0}^{K} \gamma_k \mathbf{a}(\theta_k) x(nT_s - \tau_k) + \mathbf{n}'[n].$$
(23)

The covariance matrix of the effective non-Gaussian noise  $\mathbf{n}'$  is given by

$$\begin{split} \mathbf{R}_{\mathbf{n}'\mathbf{n}'} &= \mathbf{R}_{\mathbf{e}\mathbf{e}} + \mathbf{D}\mathbf{R}_{\mathbf{n}\mathbf{n}}\mathbf{D}^* \\ &= \mathbf{R}_{\mathbf{q}\mathbf{q}} - \mathbf{R}_{\mathbf{q}\mathbf{y}}\mathbf{R}_{\mathbf{y}\mathbf{y}}^{-1}\mathbf{R}_{\mathbf{y}\mathbf{q}} + \mathbf{R}_{\mathbf{q}\mathbf{y}}\mathbf{R}_{\mathbf{y}\mathbf{y}}^{-1}\mathbf{R}_{\mathbf{n}\mathbf{n}}\mathbf{R}_{\mathbf{y}\mathbf{y}}^{-1}\mathbf{R}_{\mathbf{y}\mathbf{q}}. \end{split} \tag{24}$$

Next, we assume that the noise term in (23) is Gaussian distributed with the same covariance as  $\mathbf{R}_{\mathbf{n'n'}}$  in (24) and use (19) to get a lower bound on the Fisher information matrix.

We note here that for the case of 1-bit ADCs, the matrix  $\mathbf{R}_{\mathbf{q}\mathbf{q}}$  is given by the classical *arcsin law* [10]

$$\mathbf{R_{qq}} = \frac{2}{\pi} \left[ \arcsin \left( \operatorname{diag}(\mathbf{R_{yy}})^{-\frac{1}{2}} \mathbf{R_{yy}} \operatorname{diag}(\mathbf{R_{yy}})^{-\frac{1}{2}} \right) \right]. \tag{25}$$

The arcsin operation is applied element-wise to the real and imaginary parts of its matrix argument. The cross-correlation matrix  $\mathbf{R}_{\mathbf{q}\mathbf{y}}$  in case of 1-bit ADCs is given by [10]

$$\mathbf{R_{qy}} = \sqrt{\frac{2}{\pi}} \operatorname{diag}(\mathbf{R_{yy}})^{-\frac{1}{2}} \mathbf{R_{yy}}.$$
 (26)

At low per-antenna SNR, the correlation matrix of the RX signal  $\mathbf{R_{yy}}$  is dominated by noise. For example, at a per-antenna SNR  $\leq -10 \text{dB}$  (which is true for practical applications at mmWave frequencies as shown in Section VII), the approximation error is less than 10% in the Frobenius norm sense. Under this approximation

$$\mathbf{R_{vv}} \approx \mathbf{R_{nn}} = \sigma^2 \mathbf{I}. \tag{27}$$

Consequently  $\mathbf{R}_{\mathbf{q}\mathbf{q}} = \mathbf{I}$  in (25),  $\mathbf{R}_{\mathbf{q}\mathbf{y}} = \sqrt{\frac{2}{\pi}}\sigma\mathbf{I}$  in (26) and  $\mathbf{D} = \sqrt{\frac{2}{\pi}}\frac{1}{\sigma}\mathbf{I}$  in (21). Combining these assertions with (24), the central second-order moment of the quantized observation vector  $\mathbf{q}[n]$  in (23) is given by

$$\mathbf{R}_{\mathbf{n}'\mathbf{n}'} = \mathbf{I}.\tag{28}$$

Since the distortion e in (20) is uncorrelated with the signal component, the mean of the signal component in (23) for the Gaussian system approximation to the non-Gaussian 1-bit system,  $\mu_{\mathbf{q}}(\psi)$ , is given by

$$\mu_{\mathbf{q}}(\boldsymbol{\psi}) = \sqrt{\frac{2}{\pi}} \frac{1}{\sigma} \mathbf{I} \underbrace{\sum_{k=0}^{K} \gamma_k \mathbf{a}(\theta_k) x(nT_s - \tau_k)}_{\boldsymbol{\mu}_{\mathbf{Y}}(\boldsymbol{\psi})}.$$
 (29)

Here  $\mu_y(\psi)$  is the mean of the received signal y in (2) before 1-bit quantization. Combining the results of (28) and (29), the lower bound to the FIM for the 1-bit quantized case under the low SNR assumption,  $\mathbf{F}_{1\text{-bit}}$ , can be computed using (19) as

$$\mathbf{F}_{1\text{-bit}} \succeq 2\text{Re} \left[ \sqrt{\frac{2}{\pi}} \frac{1}{\sigma} \left( \frac{\partial \boldsymbol{\mu}_{\mathbf{y}}(\boldsymbol{\psi})}{\partial \boldsymbol{\psi}} \right)^* \mathbf{I}^{-1} \sqrt{\frac{2}{\pi}} \frac{1}{\sigma} \left( \frac{\partial \boldsymbol{\mu}_{\mathbf{y}}(\boldsymbol{\psi})}{\partial \boldsymbol{\psi}} \right) \right]$$

$$= \frac{2}{\pi} \frac{2}{\sigma^2} \text{Re} \left[ \left( \frac{\partial \boldsymbol{\mu}_{\mathbf{y}}(\boldsymbol{\psi})}{\partial \boldsymbol{\psi}} \right)^* \left( \frac{\partial \boldsymbol{\mu}_{\mathbf{y}}(\boldsymbol{\psi})}{\partial \boldsymbol{\psi}} \right) \right] \stackrel{(a)}{=} \frac{2}{\pi} \mathbf{F}_{\text{ideal}},$$
(30)

where (a) follows from the matrix representation of (17) after accounting for the  $\frac{2}{\pi}$  factor.  $\mathbf{F}_{\text{ideal}}$  denotes the FIM for the case of an ideal ADC with infinite resolution. The details of the computation of the derivative  $\frac{\partial \mu_{y}(\psi)}{\partial \psi}$  are given in Appendix A. Comparing (30) to (16) and (17) from Section III-A, it can be seen that the FIM derived using the lower bound in (18) equals the exact Fisher information obtained using (4) at low SNRs for the 1-bit system with AWGN. The corresponding 1-bit CRB given by

$$CRB_{1-bit} \approx \frac{\pi}{2} CRB_{ideal},$$
 (31)

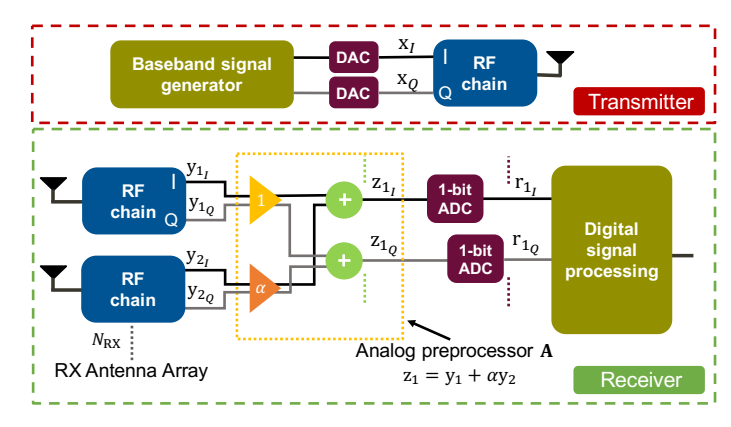


Fig. 2: The functional TX and RX block diagram with the proposed analog preprocessing structure using a simple addition of two consecutive RF chains after undergoing through a complex gain  $\alpha$ . The subscripts I and Q denote the in-phase and quadrature parts of the RF chains.

gives the same result as Section III-A that 1-bit quantization causes an estimation error performance loss of a factor of  $2/\pi \approx 2 \mathrm{dB}$  compared to an ideal unquantized system.

#### IV. ANALOG PREPROCESSOR

Improved performance as a result of correlated noise in 1bit ADC based communication and positioning systems has been observed in prior work [10], [11], [13]. Inspired by this, we design an analog preprocessing stage that beamforms in a direction of interest depending on the radar operation. As a result of the proposed preprocessor, the noise in the system becomes correlated across consecutive RF chains. The TX and RX structure with the proposed analog preprocessor are shown in Fig. 2. The top part of Fig. 2 shows the functional blocklevel description of TX side. We assume a perfect digitalto-analog converters (DAC) and a single RF chain on the TX side for now. The extension to multiple TX chains with low-resolution DACs is deferred to future work. The bottom part of Fig. 2 shows the detailed architecture of the RX side where the neighboring RF chains  $y_i$  for  $i \in 1, 2 ... N_{RX}$  after down-conversion to baseband are passed through two analog complex gains  $\alpha_1$ ,  $\alpha_2$  and then added together. We will show in Section VI-C that the optimal complex gains  $\alpha_1$  and  $\alpha_2$ can be implemented using low resolution phase shifters thus making the proposed preprocessor very easy to implement in hardware. For  $\hat{i} = \text{mod}(i + 1, N_{RX})$ , the output of the preprocessing stage  $z_i$  for  $i \in 1, 2 \dots N_{RX}$  is then given by

$$z_i = \alpha_1 y_i + \alpha_2 y_{\hat{i}}. (32)$$

The modulus operation is necessary for  $i = N_{\rm RX}$ , signifying that the last output of the preprocessing stage is obtained from the first and last RF chains.

Without loss of generality, the phase of the complex gain  $\alpha_1$  can be taken equal to 0 because it is the relative phase difference of  $\alpha_1$  and  $\alpha_2$  that's important and not their absolute phases. Because of 1-bit quantization, the absolute magnitudes of  $\alpha_1$  and  $\alpha_2$  are also not important. We fix  $\alpha_1=1$  and restrict  $0 \leq |\alpha_2| \leq 1$ . Having  $|\alpha_1| > 1$  or  $|\alpha_2| > 1$  would not change

the SNR in any way. However, it would correspond to having active power elements in the circuit. From here onwards, we use the symbol  $\alpha$  instead of  $\alpha_2$  for ease of exposition. Defining  ${\bf A}$  to be the  $N_{\rm RX} \times N_{\rm RX}$  preprocessing matrix

$$\mathbf{A} = \begin{bmatrix} 1 & \alpha & 0 & \dots & 0 \\ 0 & 1 & \alpha & \ddots & 0 \\ 0 & \ddots & \ddots & \ddots & 0 \\ \vdots & \ddots & \ddots & 1 & \alpha \\ \alpha & 0 & \dots & 0 & 1 \end{bmatrix}, \tag{33}$$

the signal vector  $\mathbf{z}(t)$  at the output of the preprocessor is given by

$$\mathbf{z}(t) = \mathbf{A}\mathbf{y}(t) = \sum_{k=0}^{K} \gamma_k \mathbf{A}\mathbf{a}(\theta_k) x(t - \tau_k) + \mathbf{A}\mathbf{n}(t). \quad (34)$$

Finally, the 1-bit quantized preprocessed signal vector sampled at the Nyquist rate is given by

$$\mathbf{r}[n] = \operatorname{sgn}(\mathbf{z}(nT_s)). \tag{35}$$

Intuition: We note here that each row of the preprocessing matrix  $\mathbf{A}$  is a  $\begin{bmatrix} 1 & \alpha \end{bmatrix}^T$  filter which beam-forms in the  $\sin^{-1}\left(-\frac{\angle\alpha\lambda}{2\pi d}\right)$  direction for  $|\alpha|=1$ . For  $\alpha=1$ , this corresponds to the  $0^\circ$  bore-sight direction. The signal and the spatially white Gaussian noise are both shaped by the frequency response of the  $\begin{bmatrix} 1 & \alpha \end{bmatrix}^T$  filter after the preprocessing stage. At low SNR ( $\approx \le 0$ dB), the quantization noise from the 1-bit ADCs is spread uniformly over the spatial domain. The SNR of the reflected path from the  $\sin^{-1}\left(-\frac{\angle\alpha\lambda}{2\pi d}\right)$  direction, however, effectively doubles after the  $\begin{bmatrix} 1 & \alpha \end{bmatrix}^T$  filter thus giving an overall gain in this direction. We explain this more formally and derive the resulting CRB in Section V and Section VI.

The preprocessing operation (denoted by  $\bf A$ ) makes the AWGN  $\bf n(t)$  correlated across any triplet of the preprocessed outputs  $z_i$ . Letting  $\tilde{\bf n}(t)$  denote the correlated noise  $\bf An(t)$ , its covariance matrix  $\bf R_{\tilde{\bf n}\tilde{\bf n}}$  is given by

$$\mathbf{R}_{\tilde{\mathbf{n}}\tilde{\mathbf{n}}} = \mathbf{A}\mathbf{R}_{\mathbf{n}\mathbf{n}}\mathbf{A}^* \qquad \text{applied element-wise to the real and imaginary parts of gument } (\cdot), \text{ the matrix } \mathbf{R}_{\mathbf{rr}} \text{ under the low SNR approxi is given by the arcsin law } [10]$$

$$= \sigma^2 \begin{bmatrix} 1 + |\alpha|^2 & \alpha & 0 & \dots & \alpha^* \\ \alpha^* & 1 + |\alpha|^2 & \alpha & \ddots & 0 \\ 0 & \ddots & \ddots & \ddots & 0 \\ \vdots & \ddots & \ddots & 1 + |\alpha|^2 & \alpha \\ \alpha & 0 & \dots & \alpha^* & 1 + |\alpha|^2 \end{bmatrix} . \qquad \mathbf{R}_{\mathbf{rr}} = \frac{2}{\pi} \left[ \operatorname{arcsin} \left( \operatorname{diag}(\mathbf{R}_{\mathbf{z}\mathbf{z}})^{-\frac{1}{2}} \mathbf{R}_{\mathbf{z}\mathbf{z}} \operatorname{diag}(\mathbf{R}_{\mathbf{z}\mathbf{z}})^{-\frac{1}{2}} \right) \right] \\ \approx \frac{2}{\pi} \left[ \operatorname{arcsin} \left( \operatorname{diag}(\mathbf{R}_{\tilde{\mathbf{n}}\tilde{\mathbf{n}}})^{-\frac{1}{2}} \mathbf{R}_{\tilde{\mathbf{n}}\tilde{\mathbf{n}}} \operatorname{diag}(\mathbf{R}_{\tilde{\mathbf{n}}\tilde{\mathbf{n}}})^{-\frac{1}{2}} \right) \right]$$

$$= (36) \qquad \qquad \begin{bmatrix} 1 & f(\bar{\alpha}) & 0 & \dots & f(\bar{\alpha}^*) \end{bmatrix}$$

Remark 1. Note that for  $\alpha=1$ , the preprocessing stage corresponds to a  $[1 \ 1]^T$  beamformer and has nulls in the  $\theta=\pm 90^\circ$  direction. It has the effect of self-interference cancellation because the self-interference part of the RX signal in (2) jumps phase by  $\pi$  between every pair of antennas for  $\theta_0=-90^\circ$  and hence decreases the constraints on the antenna beampattern design.

#### V. IMPROVED CRB

The computation of the exact CRB in Section III-A was primarily made possible due to the product form of the likelihood  $p(\mathbf{q}|\mathbf{s}(\boldsymbol{\psi}))$  in (5). The preprocessing stage introduced in Section IV makes the noise correlated. Computing the exact CRB given by (4) essentially amounts to enumerating all the  $2^{N_{\rm RX}}$  possibilities of the quantized observation vector  $\mathbf{r}[n]$  which makes it computationally inhibitive. The analytical intractability of the FIM in the case of correlated noise and the tightness of the Gaussian lower bound in an AWGN setting at low SNRs (as demonstrated in Section III) justify our use of (19) for computing the CRB with the proposed analog preprocessor. The lower bound (30) was shown to be equal to the exact FIM in (16) at low SNRs based on the Bussgang decomposition. Following the development in Section III-C, the Bussgang theorem [16] states that the preprocessed output of the non-linear 1-bit ADC r in (35) can be decomposed into a desired signal component and an uncorrelated distortion e

$$\mathbf{r} = \mathbf{D}\mathbf{z} + \mathbf{e}.\tag{37}$$

Here **D** is given by the LMMSE estimator of **r** from **z** given by  $\mathbf{R_{rz}}\mathbf{R_{zz}^{-1}}$ . The correlation matrix of the uncorrelated distortion error **e** is given by  $\mathbf{R_{ee}} = \mathbf{R_{rr}} - \mathbf{R_{rz}}\mathbf{R_{zz}^{-1}}\mathbf{R_{zr}}$ . Defining  $\mathbf{n'}[n] = \mathbf{DAn}[n] + \mathbf{e}[n]$ , the quantized preprocessed observation vector  $\mathbf{r}[n]$  in (35) can then be written as

$$\mathbf{r}[n] = \sum_{k=0}^{K} \gamma_k \mathbf{DAa}(\theta_k) x(nT_s - \tau_k) + \mathbf{n}'[n].$$
 (38)

Similar to (24), the covariance matrix of the effective non-Gaussian noise  $\mathbf{n}'$  is given by

$$\mathbf{R}_{\mathbf{n}'\mathbf{n}'} = \mathbf{R}_{\mathbf{r}\mathbf{r}} - \mathbf{R}_{\mathbf{r}\mathbf{z}} \mathbf{R}_{\mathbf{z}\mathbf{z}}^{-1} \mathbf{R}_{\mathbf{z}\mathbf{r}} + \mathbf{R}_{\mathbf{r}\mathbf{z}} \mathbf{R}_{\mathbf{z}\mathbf{z}}^{-1} \mathbf{R}_{\tilde{\mathbf{n}}\tilde{\mathbf{n}}} \mathbf{R}_{\mathbf{z}\mathbf{z}}^{-1} \mathbf{R}_{\mathbf{z}\mathbf{r}}.$$
(39)

As per the proof in [17], we assume that the noise term  $\mathbf{n'}$  in (38) is Gaussian distributed with the same covariance matrix as  $\mathbf{R}_{\mathbf{n'n'}}$  in (39). At a low per-antenna SNR, the covariance matrix of the preprocessed signal  $\mathbf{R}_{\mathbf{zz}}$  is dominated by the preprocessed noise and can be approximated as  $\mathbf{R}_{\tilde{\mathbf{n}}\tilde{\mathbf{n}}}$  given in (36). With  $\bar{\alpha} = \frac{\alpha}{1+|\alpha|^2}$  and the function  $f(\cdot) = \frac{2}{\pi} \arcsin(\cdot)$  applied element-wise to the real and imaginary parts of its argument  $(\cdot)$ , the matrix  $\mathbf{R}_{\mathbf{rr}}$  under the low SNR approximation is given by the arcsin law [10]

$$\mathbf{R_{rr}} = \frac{2}{\pi} \left[ \arcsin \left( \operatorname{diag}(\mathbf{R_{zz}})^{-\frac{1}{2}} \mathbf{R_{zz}} \operatorname{diag}(\mathbf{R_{zz}})^{-\frac{1}{2}} \right) \right]$$

$$\approx \frac{2}{\pi} \left[ \arcsin \left( \operatorname{diag}(\mathbf{R_{\tilde{n}\tilde{n}}})^{-\frac{1}{2}} \mathbf{R_{\tilde{n}\tilde{n}}} \operatorname{diag}(\mathbf{R_{\tilde{n}\tilde{n}}})^{-\frac{1}{2}} \right) \right]$$

$$= \begin{bmatrix} 1 & f(\bar{\alpha}) & 0 & \dots & f(\bar{\alpha}^*) \\ f(\bar{\alpha}^*) & 1 & f(\bar{\alpha}) & \ddots & 0 \\ 0 & \ddots & \ddots & \ddots & 0 \\ \vdots & \ddots & \ddots & \ddots & 0 \\ \vdots & \ddots & \ddots & 1 & f(\bar{\alpha}) \\ f(\bar{\alpha}) & 0 & \dots & f(\bar{\alpha}^*) & 1 \end{bmatrix}.$$

$$(40)$$

The covariance matrix of the effective noise  $\mathbf{R_{n'n'}}$  in (39) approximately equals  $\mathbf{R_{rr}}$  under the assumption  $\mathbf{R_{zz}} \approx \mathbf{R_{\tilde{n}\tilde{n}}}$ .

Additionally, the cross-correlation matrix  $\mathbf{R_{rz}}$  in case of 1-bit ADCs is given by [10]

$$\mathbf{R_{rz}} = \sqrt{\frac{2}{\pi}} \operatorname{diag}(\mathbf{R_{zz}})^{-\frac{1}{2}} \mathbf{R_{zz}}$$

$$\approx \sqrt{\frac{2}{\pi} \left(\frac{1}{1 + |\alpha|^2}\right)} \frac{1}{\sigma} \mathbf{R_{\tilde{\mathbf{n}}\tilde{\mathbf{n}}}}.$$
(41)

Combining (41) and the approximation  $\mathbf{R}_{\mathbf{z}\mathbf{z}} \approx \mathbf{R}_{\tilde{\mathbf{n}}\tilde{\mathbf{n}}}$ , the matrix  $\mathbf{D}$  in (37) is given by  $\sqrt{\frac{2}{\pi} \left(\frac{1}{1+|\alpha|^2}\right) \frac{1}{\sigma} \mathbf{I}}$ .

Since the noise  $\mathbf{n}'$  in (38) is uncorrelated with the signal component, the mean of the signal component for the Gaussian system approximation to the non-Gaussian 1-bit system,  $\mu_{\mathbf{r}}(\psi)$ , is given by

$$\mu_{\mathbf{r}}(\boldsymbol{\psi}) = \sqrt{\frac{2}{\pi} \left(\frac{1}{1 + |\alpha|^2}\right)} \frac{1}{\sigma} \mathbf{I} \underbrace{\sum_{k=0}^{K} \gamma_k \mathbf{A} \mathbf{a}(\theta_k) x(nT_s - \tau_k)}_{\boldsymbol{\mu}_{\mathbf{z}}(\boldsymbol{\psi}) = \mathbf{A} \boldsymbol{\mu}_{\mathbf{y}}(\boldsymbol{\psi})}.$$
(42)

Here  $\mu_z(\psi)$  is the mean of the received preprocessed signal z in (34) before 1-bit quantization. Note that  $\mu_z(\psi) = A\mu_y(\psi)$ . Combining the results of (42) with  $R_{n'n'} \approx R_{rr}$ , the lower bound to the FIM for the preprocessed 1-bit quantized case under the low SNR assumption,  $F_{1\text{-bit-PP}}$ , is given by

 $\mathbf{F}_{1\text{-bit-PP}}$ 

$$\geq \frac{2}{\pi} \left( \frac{1}{1 + |\alpha|^2} \right) \frac{2}{\sigma^2} \operatorname{Re} \left[ \left( \frac{\partial \mu_{\mathbf{z}}(\psi)}{\partial \psi} \right)^* \mathbf{R}_{\mathbf{rr}}^{-1} \left( \frac{\partial \mu_{\mathbf{z}}(\psi)}{\partial \psi} \right) \right]$$

$$= \frac{2}{\pi} \left( \frac{1}{1 + |\alpha|^2} \right) \frac{2}{\sigma^2} \operatorname{Re} \left[ \left( \frac{\partial \mu_{\mathbf{y}}(\psi)}{\partial \psi} \right)^* \times \right.$$

$$\left. \mathbf{A}^* \mathbf{R}_{\mathbf{rr}}^{-1} \mathbf{A} \left( \frac{\partial \mu_{\mathbf{y}}(\psi)}{\partial \psi} \right) \right].$$

$$(43)$$

The matrices  $\mathbf{A}^*$ ,  $\mathbf{R}_{\mathbf{rr}}$ ,  $\mathbf{A}$  in (43) are circulant and hence can be diagonalized by the FFT matrix  $\mathbf{F}_{N_{\mathrm{RX}}}$  and the inverse FFT matrix  $\mathbf{F}_{N_{\mathrm{RX}}}^*$  as  $\mathbf{F}_{N_{\mathrm{RX}}}$  diag $(\mathbf{\Delta}(\cdot))\mathbf{F}_{N_{\mathrm{RX}}}^*$ , where the operator  $\mathbf{\Delta}(\cdot)$  denotes the vector of eigenvalues of the matrix  $(\cdot)$  [26]. In case of a circulant matrix, the eigenvector  $\mathbf{\Delta}(\cdot)$  is given by the FFT of the first row of the corresponding matrix, that is  $\overline{(\cdot)_1}$  [26].  $\overline{\mathbf{A}_1}$  denotes the FFT of  $\mathbf{A}_1 = [1, \alpha, 0, \dots 0]$ . The first row of  $\mathbf{A}^*$ ,  $[1, 0, \dots 0, \alpha^*]$ , equals the conjugate time-reversed version of  $\mathbf{A}_1$ . Hence,  $\overline{\mathbf{A}_1^*} = (\overline{\mathbf{A}_1})^*$ . Similarly  $\overline{(\mathbf{R}_{\mathbf{rr}})_1}$  denotes the FFT of the first row of  $\mathbf{R}_{\mathbf{rr}}$ . We note here that  $\overline{(\mathbf{R}_{\mathbf{rr}})_1} \in \mathcal{R}^{N_{\mathrm{RX}}}$  because of the complex conjugate nature of  $(\mathbf{R}_{\mathbf{rr}})_1$ . With these definitions, (43) can be simplified to

$$\mathbf{F}_{1\text{-bit-PP}} \succeq \frac{2}{\pi} \frac{2}{\sigma^2} \operatorname{Re} \left[ \left( \frac{\partial \boldsymbol{\mu}_{\mathbf{y}}(\boldsymbol{\psi})}{\partial \boldsymbol{\psi}} \right)^* \mathbf{F}_{N_{\mathrm{RX}}} \left( \frac{1}{1 + |\alpha|^2} \right) \times \operatorname{diag}((\overline{\mathbf{A}_{1}})^*) (\operatorname{diag}(\overline{(\mathbf{R}_{\mathbf{rr}})_{1}}))^{-1} \operatorname{diag}(\overline{\mathbf{A}_{1}}) \mathbf{F}_{N_{\mathrm{RX}}}^* \left( \frac{\partial \boldsymbol{\mu}_{\mathbf{y}}(\boldsymbol{\psi})}{\partial \boldsymbol{\psi}} \right) \right]. \tag{44}$$

Let  $\mathbf{R}_{PP} = \left(\frac{1}{1+|\alpha|^2}\right) diag((\overline{\mathbf{A}_1})^*) (diag(\overline{\mathbf{R}_{rr-1}}))^{-1} diag(\overline{\mathbf{A}_1}).$  We emphasize here that  $\mathbf{R}_{PP}$  is a diagonal matrix with real entries. Comparing (44) to (30), it can be seen that the FIM

for the preprocessed 1-bit quantization setup differs *only* by the factor  $\mathbf{R}_{PP}$  from the FIM for the case without preprocessing where  $\mathbf{R}_{PP} = \mathbf{I}_{N_{RX}}$  as discussed in remark 2.

*Remark* 2. For 1-bit quantization *without* preprocessing, the effect of quantization is spatially uniform on the FIM. The FIM as derived in (30) can be written as

$$\mathbf{F}_{1\text{-bit}} \succeq \frac{2}{\pi} \frac{2}{\sigma^{2}} \operatorname{Re} \left[ \left( \frac{\partial \boldsymbol{\mu}_{\mathbf{y}}(\boldsymbol{\psi})}{\partial \boldsymbol{\psi}} \right)^{*} \mathbf{F}_{N_{\mathsf{RX}}} \mathbf{I}_{N_{\mathsf{RX}}} \mathbf{F}_{N_{\mathsf{RX}}}^{*} \left( \frac{\partial \boldsymbol{\mu}_{\mathbf{y}}(\boldsymbol{\psi})}{\partial \boldsymbol{\psi}} \right) \right]$$

$$= \frac{2}{\pi} \frac{2}{\sigma^{2}} \operatorname{Re} \left[ \left( \frac{\partial \mathbf{F}_{N_{\mathsf{RX}}}^{*} \boldsymbol{\mu}_{\mathbf{y}}(\boldsymbol{\psi})}{\partial \boldsymbol{\psi}} \right)^{*} \mathbf{I}_{N_{\mathsf{RX}}} \left( \frac{\partial \mathbf{F}_{N_{\mathsf{RX}}}^{*} \boldsymbol{\mu}_{\mathbf{y}}(\boldsymbol{\psi})}{\partial \boldsymbol{\psi}} \right) \right].$$

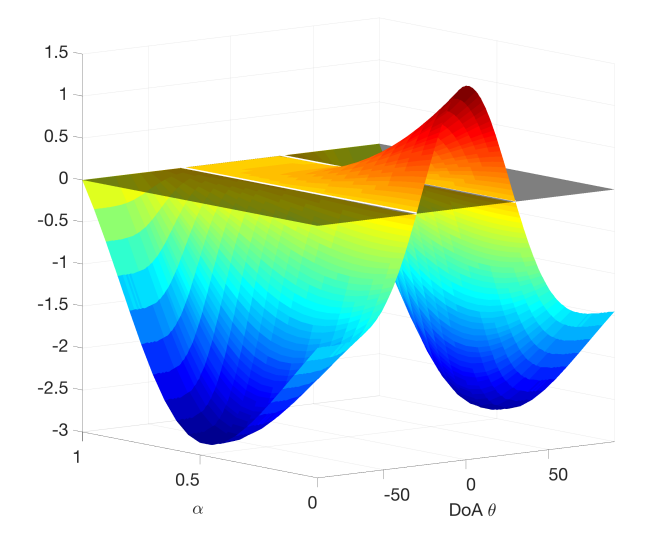
$$(45)$$

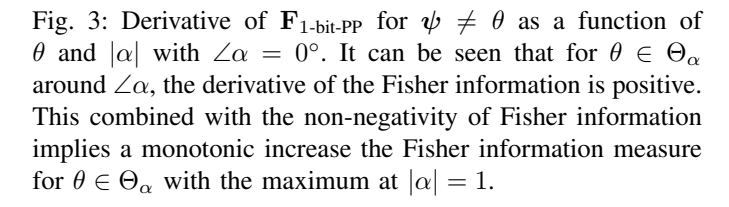
The effect of quantization on the FIM as a function of the DoA can be quantified by splitting the parameter vector  $\psi$ into two parts. For  $\psi \neq \theta$ , the vector  $\frac{\partial \mathbf{F}_{N_{\mathrm{R}}N_{\mathrm{L}}\Psi}^{\mathrm{Parther}}(\psi)}{\partial \psi}$  can be split into two parts: 1) The conjugate Fourier transform of the array response vector  $\mathbf{a}(\theta)$ , given by  $\overline{\mathbf{a}}(\theta)$ , which can be pulled out of the partial derivative operator and 2) A complex scaling given by  $\frac{\partial \alpha x(nT_s-\tau)}{\partial \psi}$ . Now consider the spatial angular grid  ${\cal A}$  corresponding to the  $N_{\rm RX}$  FFT frequencies (function of the  $N_{\mathrm{RX}}$  RX antennas and the array response vector). The  $k^{th}$  element  $\mathcal{A}_k$  is given by  $\sin^{-1}(\frac{\lambda k}{dN_{\mathrm{RX}}})$  for  $k \in \{\frac{-N_{\mathrm{RX}}}{2}\dots\frac{N_{\mathrm{RX}}}{2}-1\}$ . For a spatially *on-grid* target located at the  $k^{th}$  grid position,  $\overline{\mathbf{a}}(\theta) = \sqrt{N_{\text{RX}}} \mathbf{e}_k$ . The product  $(\overline{\mathbf{a}}(\theta))^* \mathbf{I}_{N_{\text{RX}}} \overline{\mathbf{a}}(\theta)$  thus equals  $N_{\rm RX}$  irrespective of the DoA  $A_k$  of the target. For an off-grid target with DoA  $\theta$ ,  $(\overline{\mathbf{a}}(\theta))^* \mathbf{I}_{N_{RX}} \overline{\mathbf{a}}(\theta) = N_{RX}$  by Parseval's theorem. For the case  $\psi = \theta$ , the Fisher information by definition depends on the DoA (even for ideal ∞-resolution ADCs), being the largest for  $\theta = 0^{\circ}$  (broad-side) and smallest for  $\theta=\pm90^\circ$  (end-fire). For  $\psi=\theta$ , The vector  $\frac{\partial \mathbf{F}^*_{N_{\mathrm{RX}}}\mu_{\mathbf{y}}(\psi)}{\partial \psi}$ is given by the conjugate FFT of  $\frac{\partial \mu_{\mathbf{y}}(\psi)}{\partial \theta}$  given in (52) in Appendix A. Nonetheless, it uniformly affects all spatial directions through the matrix  $I_{N_{RX}}$  and the factor  $\frac{2}{\pi}$ . Hence, perhaps not surprisingly, 1-bit quantization effects the FIM uniformly irrespective of the DoA  $\theta$  of the target.

Remark 3. For 1-bit quantization with preprocessing, the effect of the preprocessing and quantization is a function of the choice of  $\alpha$  and the DoA  $\theta$  of the target. For  $k \in \{0 \dots N_{\rm RX} - 1\}$ , the dependence of the  $k^{th}$  entry along the diagonal of  $\mathbf{R}_{\rm PP}$  on  $\alpha$  is given by

$$(\mathbf{R}_{PP})_{kk} = \left(\frac{1}{1+|\alpha|^2}\right) \times \frac{1+|\alpha|^2 + \alpha e^{j2\pi k/N_{RX}} + \alpha^* e^{-j2\pi k/N_{RX}}}{1+f(\bar{\alpha})e^{j2\pi k/N_{RX}} + f(\bar{\alpha}^*)e^{-j2\pi k/N_{RX}}}.$$
(46)

Here k=0 corresponds to the first and  $k=N_{\rm RX}-1$  to the last entry along the diagonal. As detailed in remark 2, the DoA of the target,  $\theta$ , determines the weight assigned to the entries of  ${\bf R}_{\rm PP}$  through the product  $({\bf \bar a}(\theta)^*{\bf R}_{\rm PP}{\bf \bar a}(\theta))$ . Thus the preprocessed 1-bit quantization has a spatially *non-uniform* effect on the FIM. This encourages the optimization of the analog preprocessor from the perspective of choice of the parameter  $\alpha$  as detailed in Section VI.





### VI. PREPROCESSOR OPTIMIZATION

The FIM derived for the analog preprocessor architecture in Section V,  $\mathbf{F}_{\text{1-bit-PP}}$ , leaves open the question of the choice of the parameter  $\alpha$ . In this section, we provide design rules for the choice of  $\alpha$  and discuss results for different values of  $\alpha$ .

# A. Optimization of $|\alpha|$

The proposed analog preprocessor and the FIM (44) derived based on that structure do not provide any guidelines about the choice of  $|\alpha|$ . For the remainder of this subsection we assume that  $\angle \alpha = 0^{\circ}$  and leave the details of the optimization of  $\angle \alpha$  to Section VI-B. Let  $\mathbf{R}'_{PP}$  denote the derivative of  $\mathbf{R}_{PP}$  with respect to (WRT)  $|\alpha|$ . The details of the calculation of  $\mathbf{R}'_{PP}$  are given in Appendix B. The derivative of the Fisher information w.r.t  $|\alpha|$  of the preprocessed 1-bit system for  $\psi \neq \theta$  is shown in Fig. 3. Any constant parameters which do not depend on  $\alpha$  have been taken to be equal to unity since they do not affect the optimization WRT  $|\alpha|$ . Particularly, the expression

$$\operatorname{Re}\left[\mathbf{a}(\theta)^*\mathbf{F}_{N_{\mathrm{RX}}}\mathbf{R}_{PP}'\mathbf{F}_{N_{\mathrm{RX}}}^*\mathbf{a}(\theta)\right]$$

is plotted in Fig. 3 as a function of the spatial DoA  $\theta$  and  $0 \le |\alpha| \le 1$ . Similarly for the case of  $\psi = \theta$ , the expression

$$\operatorname{Re}\left[\left(\frac{\partial \mathbf{a}(\theta)}{\partial \theta}\right)^* \mathbf{F}_{N_{\mathrm{RX}}} \mathbf{R}_{PP}' \mathbf{F}_{N_{\mathrm{RX}}}^* \frac{\partial \mathbf{a}(\theta)}{\partial \theta}\right]$$

is illustrated in Fig. 4 as a function of the spatial DoA  $\theta$  and  $|\alpha|$ . A constant reference surface with a value of 0 is also plotted (in black) in Fig. 3 and Fig. 4. A number of observations can be made from Fig. 3 and Fig. 4. First off, the derivative of the Fisher information measure  $\rightarrow 0$  as

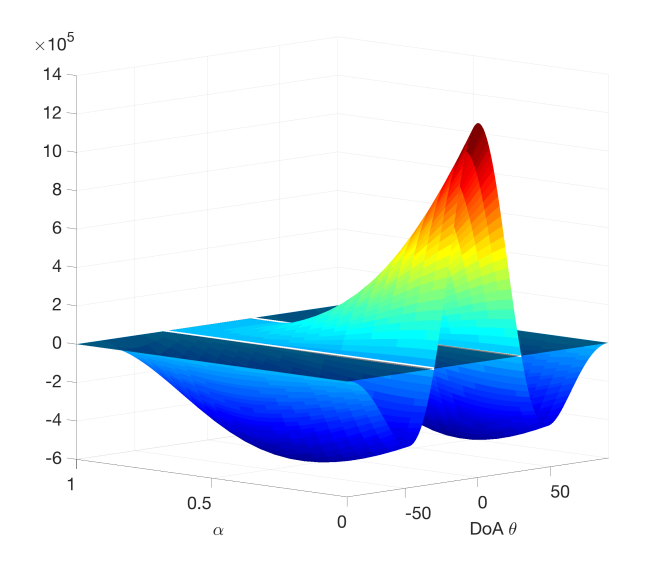


Fig. 4: Derivative of  $\mathbf{F}_{1\text{-bit-PP}}$  for  $\psi = \theta$  as a function of  $\theta$  and  $|\alpha|$  with  $\angle \alpha = 0^{\circ}$ . Similar to Fig. 3, the positive values of the derivative imply a monotonic increase in the DoA Fisher information for  $\theta \in \Theta_{\alpha}$  with the maximum occurring at  $|\alpha| = 1$ . The derivative equals 0 for  $\theta = \pm 90^{\circ}$  because the aperture size is reduced to 0 for end-fire directions.

 $|\alpha| \to 1$ . This implies that  $|\alpha| = 1$  is a stationary point irrespective of the DoA  $\theta$ . It can be seen that the derivative of the Fisher information measure is positive for a subset of DoA  $\theta \in [-\theta_{\alpha}, \theta_{\alpha}]$ , where  $\theta_{\alpha}$  is some constant that depends on  $\alpha$ . Let  $\Theta_{\alpha}$  represent the set of the DoAs  $[-\theta_{\alpha}, \theta_{\alpha}]$ . The positive values of the derivative of Fisher information for  $\theta \in \Theta_{\alpha}$  combined with the *non-negativity* of the Fisher information imply a *monotonic* increase in the Fisher information measure reaching its maximum at  $|\alpha| = 1$  for  $\theta \in \Theta_{\alpha}$ . For  $\theta \notin \Theta_{\alpha}$ , the derivatives illustrated in Fig. 3 and Fig. 4 become negative thus suggesting a decrease in the Fisher information measure  $\theta \notin \Theta_{\alpha}$  reaching its minimum at  $|\alpha| = 1$ . This suggests that the preprocessing is optimized at  $|\alpha| = 1$  for  $\theta \in \Theta_{\alpha}$  resulting in the maximum improvement that can be achieved under the proposed preprocessing architecture.

Remark 4. It can be observed from Fig. 4 that for  $\psi=\theta$ , the value of the derivative equals 0 for  $\theta=\pm90$  irrespective of  $|\alpha|$ . This is explained by the fact that  $\theta=\pm90$  corresponds to the end-fire direction with reference to the array. The Fisher information measure is 0 for  $\theta=\pm90$  even in the case of ideal ADCs. This is so because the aperture size reduces to 0 for  $\theta=\pm90$ . The proposed preprocessing can not further change that.

#### B. Optimization of $\angle \alpha$

Fig. 3 and Fig. 4 provide a hint towards the optimization of  $\angle \alpha$ . It can be seen that the derivative of the FIM is positive in a set  $\Theta_{\alpha}$  centered around  $\angle \alpha = 0^{\circ}$ . Consequently the preprocessed FIM improves over the unprocessed case in this set  $\Theta_{\alpha}$  attaining the maximum improvement for  $\theta = 0^{\circ}$ 

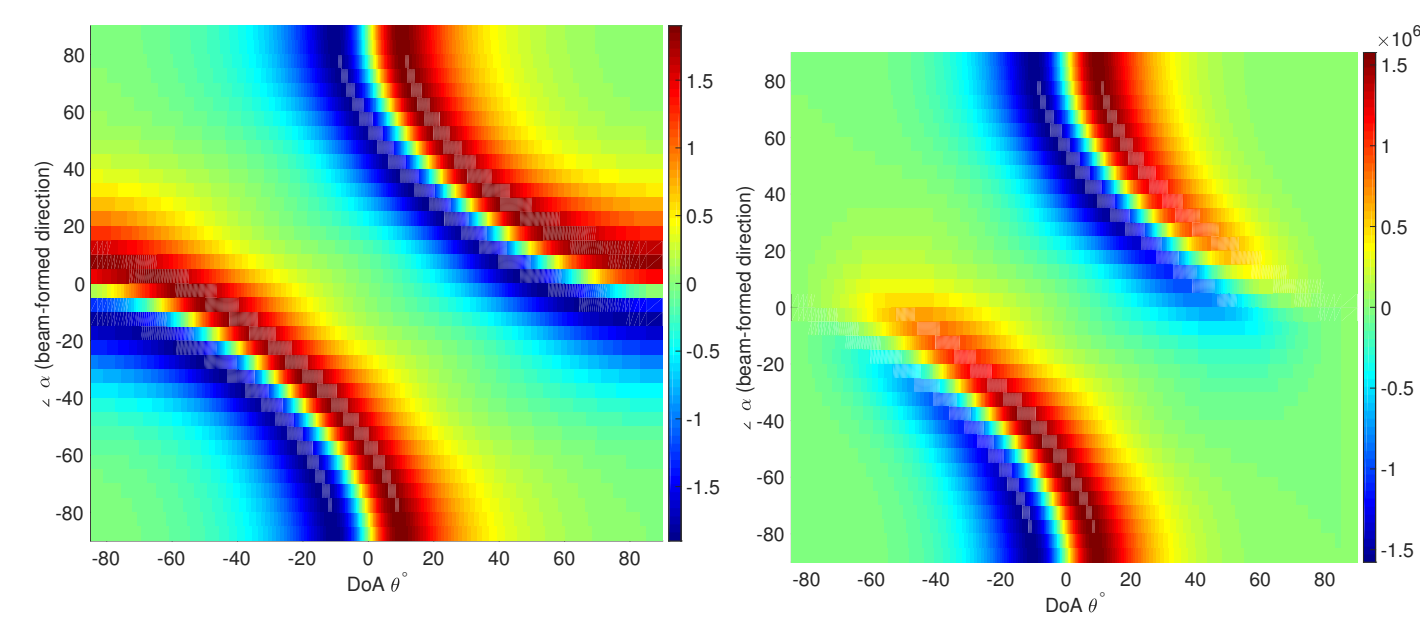


Fig. 5: Derivative of  $\mathbf{F}_{1\text{-bit-PP}}$  for  $\psi \neq \theta$  as a function of  $\theta$  and  $\angle \alpha$  with  $|\alpha|=1$ . It can be seen that the derivative equals 0 for two different values of  $\theta$  for each value of  $\angle \alpha$ . Claim 1 proves that the FIM gets the most improvement for  $\bar{\theta}=\sin^{-1}\left(-\frac{\angle\alpha\lambda}{2\pi d}\right)$ , the beamforming direction for a  $\begin{bmatrix}1&\alpha\end{bmatrix}$  filter.

where the derivative can be seen to be the largest. This makes intuitive sense because setting  $\angle \alpha = 0^{\circ}$  makes the preprocessor beamform towards  $\theta = 0^{\circ}$ .

This observation can be quantified by considering the stationary points of the FIM w.r.t  $\angle \alpha$ . Let  $\mathbf{R}''_{PP}$  be the derivative of  $\mathbf{R}_{PP}$  w.r.t  $\angle \alpha$ . The details of the computation of  $\mathbf{R}''_{PP}$  are given in Appendix C. Analogous to Fig. 3 and Fig. 4, the expressions

$$\operatorname{Re}\left[\mathbf{a}(\theta)^*\mathbf{F}_{N_{\mathsf{RX}}}\mathbf{R}_{PP}''\mathbf{F}_{N_{\mathsf{RX}}}^*\mathbf{a}(\theta)\right]$$

and

$$\operatorname{Re}\left[\left(\frac{\partial \mathbf{a}(\theta)}{\partial \theta}\right)^* \mathbf{F}_{N_{\mathrm{RX}}} \mathbf{R}_{PP}^{\prime\prime} \mathbf{F}_{N_{\mathrm{RX}}}^* \frac{\partial \mathbf{a}(\theta)}{\partial \theta}\right]$$

are illustrated in Fig. 5 and Fig. 6 as a function of the spatial DoA  $\theta$  and  $\angle \alpha$ . Having established that  $|\alpha|=1$  maximizes the FIM for  $\theta \in \Theta_{\alpha}$  in Section VI-A, we restrict  $|\alpha|=1$  for the remainder of this section. As in Section VI-A, any parameters in the computation of the FIM in (44) that do not depend on  $\angle \alpha$  are taken to be equal to unity. It can be seen from Fig. 5 that for  $\psi \neq \theta$ , the derivative of the FIM equals 0 for any  $\angle \alpha$  for two different values of  $\theta$ . Fig. 6 additionally illustrates that for  $\psi = \theta$ , the derivative of the FIM equals 0 for all  $\theta$  close to the end-fire direction. Going back to Section VI-A, this connects to the explanation given in remark 4 for Fig. 4. To establish which of the stationary points corresponds to the maximum of the FIM as a function of  $\theta$ , we look at the expression for  $(\mathbf{R}_{PP})_{kk}$  in (46) (which captures the effect of the proposed preprocessing on the FIM) in more detail.

**Claim 1.** The FIM gets the maximum improvement at  $\bar{\theta} = \sin^{-1}\left(-\frac{\angle \alpha\lambda}{2\pi d}\right)$ .

Fig. 6: Derivative of  $\mathbf{F}_{\text{1-bit-PP}}$  for  $\psi = \theta$  as a function of  $\theta$  and  $\angle \alpha$  with  $|\alpha| = 1$ . In addition to the observations made in Fig. 5, it can be seen that the derivative of the DoA Fisher information measure equals 0 for all angles close to the end-fire direction.

Proof: See Appendix D.

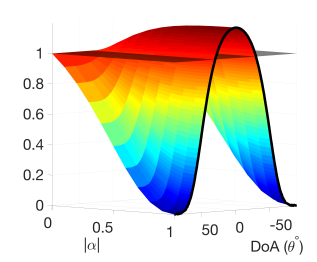
C. Analog preprocessor using low-resolution phase-shifters

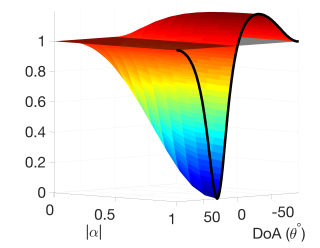
Having established that  $|\alpha|=1$  results in the maximum improvement in a subset of  $\theta\in\Theta_{\alpha}$  centered around  $\bar{\theta}=\sin^{-1}\left(-\frac{\angle\alpha\lambda}{2\pi d}\right)$ , we now understand how to choose  $\alpha$  depending on the application. For example, the field of view (FoV) of interest for a long-range radar (LRR) in an automotive setting consists of the spatial directions close to broad-side [23]. In this case,  $\alpha=1$  is the appropriate choice resulting in the maximum improvement at  $\theta=0^{\circ}$ . An adaptable high-resolution high-bandwidth  $\alpha$  would require complex circuitry that will consume a significant amount of power. In this section, we look at the improvements in FIM achievable using low-resolution phase-shifters as potential ways of choosing  $\alpha$ .

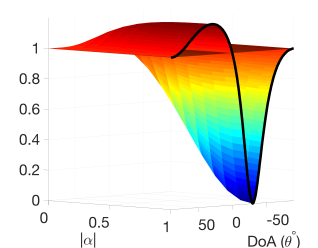
Low-resolution phase-shifters are of interest because of reduced hardware complexity, power consumption, and cost [27]. With  $\mathcal{I}_q = \{0, 1 \dots q-1\}$ , the set of phase shifts achievable by a q-bit phase shifter is given by  $\mathcal{Q}_q = \{\exp(\mathrm{j}2\pi k/2^q): k \in \mathcal{I}_q\}$ . For a specific parameter  $\psi = \psi_k$ , we define the ratio of the (k,k)-th elements of the Fisher information matrices given in (44) and (45),

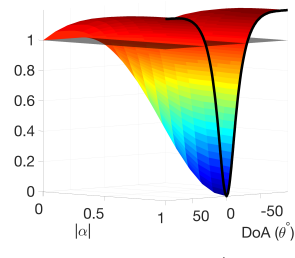
$$\chi(\theta, \alpha) = \frac{[\mathbf{F}_{1\text{-bit-PP}}]_{kk}}{[\mathbf{F}_{1\text{-bit}}]_{kk}},$$

as the gain of the preprocessed system as a function of varying  $\theta$  and  $\alpha$ . The gain  $\chi(\theta,\alpha)$  (for  $\psi \neq \theta$ ) for  $-90^{\circ} \leq \theta \leq 90^{\circ}$  and  $\alpha = |\alpha|e^{\mathrm{j}\angle\alpha}$ , where  $0 \leq |\alpha| \leq 1$  and  $\angle\alpha \in \mathcal{Q}_2$  is illustrated in Fig. 7. A 2-bit phase shifter can, in fact, be implemented through two 1-bit comparators in the real and quadrature dimensions and four switches. The four subfigures,









(a)  $\alpha = |\alpha|e^{\mathrm{j}2\pi\times0/4}$ . Maximum gain at  $\theta = 0^\circ$ .  $\chi \ge 1$  in  $\Theta_\alpha = \{0\}$  i

 $|\alpha|e^{\mathrm{j}2\pi\times2/4}$ . Maxi-(d)  $\alpha =$ mum gain at  $\dot{\theta}=\pm90^{\circ}$ .  $\chi\geq$ 1 in  $\Theta_{\alpha} = [-90^{\circ}, -30^{\circ}]$ [30°, 90°]. Null at  $\theta = 0^{\circ}$ .

Fig. 7: Improvement in FIM,  $\chi$ , as a function of the DoA  $\theta$  and  $|\alpha|$  for large  $N_{\rm RX}$ . As analyzed in section VI-A and VI-B, maximum improvement occurs for  $|\alpha| = 1$  and at around  $\theta = \sin^{-1}\left(-\frac{\angle \alpha\lambda}{2\pi d}\right)$ . The black line in each subfigure shows the 4 possible improvements resulting from the use of a 2-bit phase shifter corresponding to its 4 distinct phases.

each corresponding to one of the elements of  $Q_2$ , also illustrate a constant surface with a value of 1 as a reference. All points above this surface are where the preprocessing architecture results in improvements over the unprocessed case. Each of the subfigures also plots a black line for  $|\alpha| = 1$ , which is the resulting gain for the case of  $\alpha \in \mathcal{Q}_2$ . As analyzed in section VI-A, the maximum gain occurs at  $|\alpha| = 1$  for all values of  $\angle \alpha$  considered. This is of importance since the preprocessing architecture in Fig. 2 can now be realized through low-resolution phase-shifters. As per claim 1, the FIM gain  $\chi > 1$  in a region  $\Theta_{\alpha}$  centered at  $\bar{\theta} = \sin^{-1}\left(-\frac{\angle \alpha\lambda}{2\pi d}\right)$  in each subfigure. The region  $\Theta_{\alpha}$  is not necessarily symmetric around  $\bar{\Theta}$ . This is due to the sinusoidal dependence of spatial frequency of the array factor on the physical DoA  $\theta$ . For  $\psi = \theta$ , the gain  $\chi$  looks very much like Fig. 7 other than 2 subtleties. There is slight spreading due to the term  $\left(\frac{\partial \mathbf{a}(\theta)}{\partial \theta}\right)^* \mathbf{F}_{N_{\mathrm{RX}}}$  when  $\psi = \theta$ . Secondly at  $\theta = \pm 90^\circ$ , the gain  $\chi$  is not exactly defined because  $\mathbf{F}_{1\text{-bit-PP}} = \mathbf{F}_{1\text{-bit}} = 0$  because of zero aperture size in the end-fire direction. As hinted at the beginning of section VI-C,  $\alpha$  has a significant impact on the system performance and has to be chosen according to the application of interest. The choice of  $\alpha = 1$  with the gain  $\chi$ of Fig. 7a is appropriate for an LRR application. On the other hand, the choice of  $\alpha$  in Fig. 7b and Fig. 7c is appropriate for cross traffic alerts and use as parking sensors within the ADAS realm [22], [28].

The FIM gain  $\chi$  in Fig. 7 peaks at 1.2 for all values of  $\alpha$  considered in Fig. 7. This result follows from (65) at the optimal values of  $|\alpha|$  and  $\bar{\theta}$ . The CRB at the optimal value of  $|\alpha|$  and  $\bar{\theta}$  then follows from (44) as

$$\mathbf{CRB}_{1\text{-bit-PP}}|_{|\alpha|=1,\bar{\theta}=\sin^{-1}\left(-\frac{\angle \alpha\lambda}{2\pi d}\right)} \approx \frac{\pi}{2.4}\mathbf{CRB}_{\text{ideal}}.$$
 (47)

It follows from (47) that the preprocessed case suffers a loss of  $\frac{\pi}{2.4} \approx 1.16 \text{dB}$  in comparison to the ideal ADC case in the beamformed direction. This is an improvement of 0.8dB in comparison to the unprocessed case derived in (31).

*Note:* The analog preprocessor, its optimization and the resulting improvements from it have all been confined to the specific structure shown in Fig. 2. A more general analog preprocessor which beamforms in any specific direction using n neighboring RF chains can achieve a higher gain in and around the beamformed direction. This is, however, a game of diminishing returns with the highest return coming at the first step, i.e. n=2, as discussed in this paper. This resembles the effect of oversampling that has been observed in [14] and [13]. A more general beamforming architecture will also strongly affect the results shown in Fig. 7 by introducing local minimums and maximums.

#### VII. RESULTS AND DISCUSSION

The performance of the proposed architecture for the case of ideal infinite resolution ADCs and 1-bit ADCs derived in Section III and 1-bit ADCs with analog preprocessing derived in Section V is characterized by numerically evaluating the CRB for each case. We emphasize here that the low-SNR assumption  $R_{yy} \approx R_{nn}$  in Section III and  $R_{zz} \approx R_{n'n'}$ in Section V is dropped in the numerical computation of the CRBs. Thus, we expect deviation from the results derived in this paper at medium to high SNRs. The important simulation parameters, summarized in Table I, are inspired from an automotive setting [22], [23]. We take the transmit power  $P_t$ to be 20dBm. The numerical evaluations are done for a TX antenna gain of 13dBi, RX antenna gain of 5dBi, target RCS  $\zeta$  of 0dBsm, a bandwidth of 1 GHz, a RX antenna array of 64 elements and a CPI of 100 IID symbols. The results illustrated in this Section are for  $\alpha = 1$  and correspond to the gain observed in Fig. 7a with maximum improvement at  $\theta = 0^{\circ}$ . Results similar to what is presented for  $\alpha = 1$  are obtained for other choices of  $\alpha$ . We first present CRB results for the

Bandwidth $B$	1 GHz
Carrier frequency $f_c$	77 GHz
Transmit power	20 dBm
TX antenna gain	13 dBi
RX antenna gain	5 dBi
Path loss coefficient	2
Target RCS ζ	0 dBsm
Number of RX array elements $N_{RX}$	64
Number of TX symbols L	100

TABLE I: Important simulation parameters

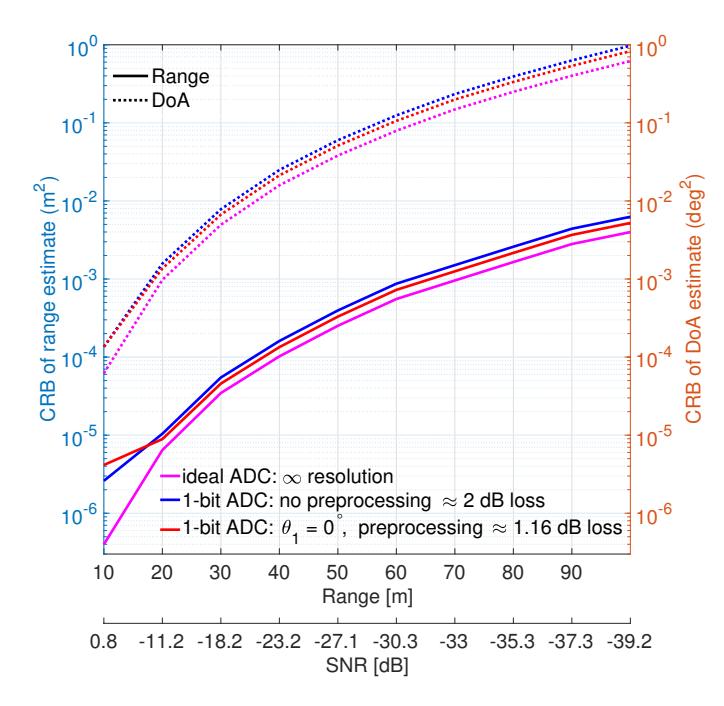


Fig. 8: The CRB of the range and DoA estimate for the case of an ideal ADC and 1-bit ADC with and without the proposed preprocessing (for  $\alpha=1$ ) for a target located at  $\theta_1=0^\circ$ . At low per-antenna SNRs, the introduction of the preprocessor results in an improvement of .84dB. At mid-range SNRs the  $\mathbf{R_{yy}} \approx \mathbf{R_{nn}}$  assumption does not remain true and the CRBs for both 1-bit quantized systems start to deviate from the ideal ADC case. Best viewed in color.

two parameters of interest: 1) Range and 2) DoA in single target and multi-target settings followed by the improvement in MSE for a simple correlation-based range-DoA estimator.

#### A. CRB results

# 1) Single target setting

The CRB for the target range (in solid) and DoA (in dotted) estimation error against the true target position for a single target setting is illustrated in Fig. 8. The target position is changed in increments of 10 m from 10 m to 100 m whereas its DoA is held fixed at  $0^{\circ}$ . The target distance maps from a maximum target (per-antenna) SNR of about 0dB at 10 m to a minimum target SNR of -40dB at 100 m shown as a second x-axis in Fig. 8.

The solid magenta line (\_\_\_\_) in Fig. 8 is the range CRB for the system with infinite resolution ADCs which is inversely proportional to the fourth power of the target range. This is coherent with the result derived in [1]. The solid blue line (\_\_\_\_) in Fig. 8 is for the case of 1-bit ADCs which only observe the sign of the RX signal. As derived in (31), the CRB for the 1-bit case suffers a loss of  $\frac{\pi}{2} \approx 2 dB$  at low SNRs. At high SNRs the assumption  $\mathbf{R_{yy}} \approx \mathbf{R_{nn}}$  is violated and (27) does not hold anymore. As a result, the 1-bit CRB starts to diverge from the CRB for ideal ADCs at smaller ranges as seen in Fig. 8. Interestingly enough, at mmWave frequencies, the per-antenna operating SNR falls in the low

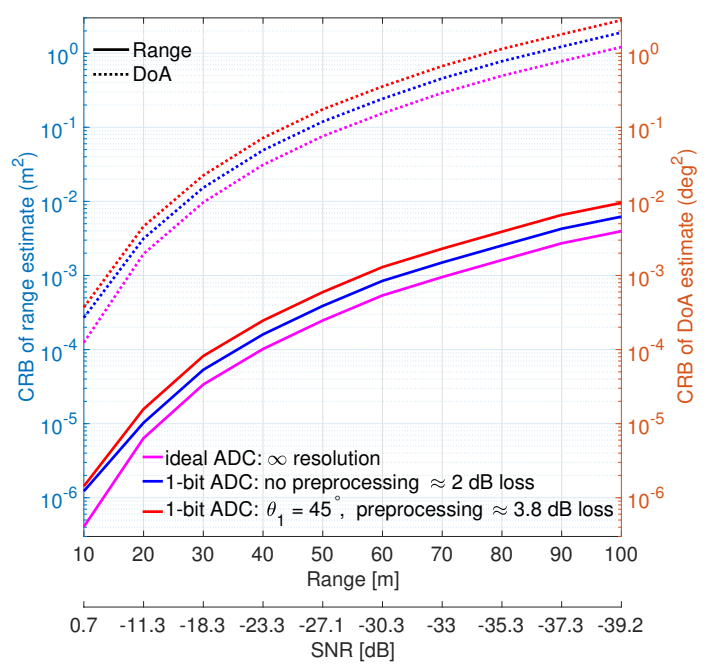


Fig. 9: The CRB for the range and DoA estimate for the case of an ideal ADC and 1-bit ADC with and without the proposed preprocessing (for  $\alpha=1$ ) for a target located at  $\theta_1=45^\circ$ . It can be seen that the proposed preprocessing suffers a loss (in agreement with Fig. 7a) compared to the case without preprocessing because  $\theta_1=45^\circ\notin\Theta_\alpha$  for  $\alpha=1$ . Best viewed in color.

SNR regime thus making the bound (31) useful. The new results derived in this paper using the analog preprocessing unit shown in Fig. 2 with 1-bit ADCs are shown in the solid red line (\_\_\_) in Fig. 8. For  $\alpha = 1$ , the proposed analog beamformer in (33) coherently adds the target contributions of RX signal over neighboring RF chains for  $\theta_1 = 0^{\circ}$ . As per (47), the CRB for the 1-bit preprocessed case suffers a loss of  $\frac{\pi}{2.4} \approx 1.16 \mathrm{dB}$  from the ideal ADC case at low SNRs. It can be observed that the system with preprocessing starts to deviate from the ideal ADC system earlier compared to the case without analog preprocessing. This happens because for a target at  $\theta_1 = 0^{\circ}$ , the signal power is increased by a factor of 4 after the preprocessing stage boosting the SNR by a factor of 2. The  $\mathbf{R_{zz}} \approx \mathbf{R_{n'n'}}$  condition is thus violated earlier for the architecture with preprocessing which explains the crossover between the red and blue lines in Fig. 8. We point out here that this artifact can be removed by introducing a switching network in Fig. 2 which takes the preprocessing network out of the system at mid-range SNRs or by dithering but we do not pursue this further in this work. Similar observations about the DoA CRB can be made from the set of three dotted (......) lines shown in Fig. 8.

Fig. 9 illustrates results for a setting similar to Fig. 8 except that the target is now placed at  $\theta_1 = 45^\circ$ . It follows from Fig. 7a that  $\chi(45^\circ,1) \leq 1$ , resulting in the preprocessed CRB being larger than the case without preprocessing. The solid magenta (\_\_\_) and blue (\_\_\_) lines in Fig. 9 equal their counterparts in Fig. 8. However, the solid red line (\_\_\_) in

Fig. 9 corresponding to the range CRB for the preprocessed case experiences a loss larger than simple 1-bit quantization in contrast to its counterpart in Fig. 8, thus confirming the earlier observation. The reason is that for  $\alpha = 1$ , the proposed analog preprocessor does not coherently add the signals for a target located at  $\theta_1 = 45^{\circ}$ . The same observation can be made for the set of dotted (......) lines which correspond to the DoA CRB. The dotted lines in Fig. 9 suffer an additional loss in comparison to the dotted lines in Fig. 8 due to the reduced aperture length at  $\theta_1 = 45^{\circ}$ . Fig. 9 confirms the observation made in Fig. 7 that  $\alpha$  has a significant effect on the system performance and needs to be chosen depending on the radar region of interest.

#### 2) Multi-target setting

Here we present results for a two target setting where the first target is moved in increments of 10 m at  $\theta_1 = 0^{\circ}$ as in Fig. 8. The second target is held fixed at 40 m and  $\theta_2 = 2^\circ$  for all positions of the first target.  $\theta_2 = 2^\circ$  at 40 m corresponds to a cross-range separation of 1.4 m which approximately equals the half-lane width of a typical road. Hence, the two targets can be thought of as two vehicles going in two lanes next to each other. The CRB of the DoA estimate for the two targets are plotted in Fig. 10. The set of three solid (\_\_\_) lines (with same color coding as before) correspond to the first target along  $\theta_1 = 0^{\circ}$ . The three dotted lines (......) correspond to the second target with  $\theta_2 = 2^{\circ}$ . The black dashed (\_\_\_) line in Fig. 10 illustrates the DoA CRB for the single target setting from Fig. 8 for comparison. It can be observed that preprocessing results in an improvement over 1-bit quantization for both targets similar to the single target setting in Fig. 8. The CRBs for both targets increase slightly as they approach closer to each other. This makes intuitive sense as it becomes increasingly difficult to resolve the two targets as they come close to each other. The CRB for target 1 (\_\_\_) equals the CRB for the single target setting (\_ \_ \_) except in the region where the two targets are relatively close.

The range and DoA CRB results demonstrated in this section establish that the proposed architecture with 1-bit ADCs and phase-shifters performs within 1.16dB of an architecture with ideal ADCs and is capable of achieving sub-meter and sub-degree accuracy in terms of range and DoA estimation error. Hence, it is a promising candidate for future low-cost low-power consumption high-resolution sensing applications. Now we demonstrate the achievability of the improved CRB through a correlation-based estimator.

# B. Range and DoA estimator

The proposed correlation-based range and DoA estimator follow the development in [30] and [1, Ch. 7]. The maximum likelihood estimate (MLE) of delay for the discrete RX signal (at one of the RX antennas)  $y[\ell]$  for  $\ell \in \mathcal{T}$  leads to the correlation-based estimator  $\hat{\tau} = \hat{\ell}_0 T_s$  where

$$\hat{\ell}_0 = \operatorname*{argmax}_{\ell_0} \left[ \left| \sum_{\ell \in \mathcal{T}} y[\ell] s^* [\ell - \ell_0] \right| \right], \tag{48}$$

 $0 \le \ell_0 \le \lceil \frac{T + au_{\max}}{T_s} \rceil$  and  $s[\ell - \ell_0] = 0$  for  $\ell - \ell_0 \le 0$  and  $\ell - \ell_0 > L$ . An obvious problem with this estimator, especially

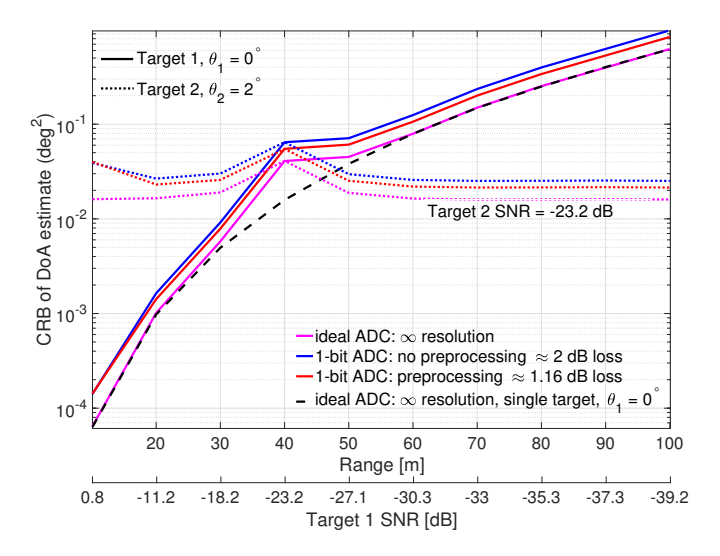


Fig. 10: Range and DoA CRB results for a two target setting. Target 1 is moved from 10 m to 100 m in increments of 10 m with its DoA  $\theta_1 = 0^{\circ}$ . Target 2 is held at 40 m and  $\theta_2 = 2^{\circ}$ . It can be seen that the proposed digital architecture preserves the flexibility provided by a fully digital architecture while reducing the performance loss due to 1-bit quantization in the region of interest. Best viewed in color.

at high SNRs, is that accuracy of the estimate is limited by the sampling time  $T_s$  since the true range estimate can lie anywhere on the real line. Assuming that the resulting error is uniformly distributed in between  $(\hat{\ell} - \frac{1}{2})T_s$  and  $(\hat{\ell} + \frac{1}{2})T_s$  leads to the simple sampling error bound  $\frac{T_s^2}{12} \left(\frac{c}{2}\right)^2$  for the range estimate [1, Ch. 7]. The estimation accuracy can be improved beyond this sampling bound (SB) by either oversampling the RX signal or interpolating the RX signal/correlation statistics to a higher rate [1], [30]. Since the sampling frequency is limited by hardware, we resort to interpolating the RX signal before correlation. The interpolation procedure leads to increased memory and computational cost and thus can only be done to a certain degree as the sampling-based range error bound is quite far from the range CRB at relatively higher SNRS as show in Fig. 11. An alternative approach studied in [1, Ch. 7] and [30] consists of refining the correlation peak position by fitting a parabola around  $\ell_0$  in a least squares (LS) sense and taking the apex of the parabola (given by -b/2a for a parabola parametrized as  $ax^2+bx+c$ ) as the refined estimate.

# **Algorithm 1** Correlation-based range-DoA estimator

Input:  $Y, \Theta, s$ 

- 0) Pre-whiten Y (for the preprocessed case)
- 1) 2D correlation matrix R:

$$\mathbf{R}_{ij} = \sum_{m=1}^{N_{RX}} \sum_{\ell \in \mathcal{T}} \mathbf{Y}_{ln} s^* [\ell - i] \mathbf{a}(\Theta_i) [n]$$

 $\mathbf{R}_{ij} = \sum_{n=1}^{N_{\mathrm{RX}}} \sum_{\ell \in \mathcal{T}} \mathbf{Y}_{ln} s^* [\ell - i] \mathbf{a}(\Theta_j)[n]$ 2) **CFAR detection:** (Get list of potential targets)  $TargetList = CFAR(|\mathbf{R}|)$ (using [29])(coarse estimate)

3)Parabolic refinement: (For all elements in TargetList)

LeastSquares(x) for  $x \in \text{TargetList}$  (Parabola LS fitting) ApexCalculation(LS(x))(see [30])(refined estimate)

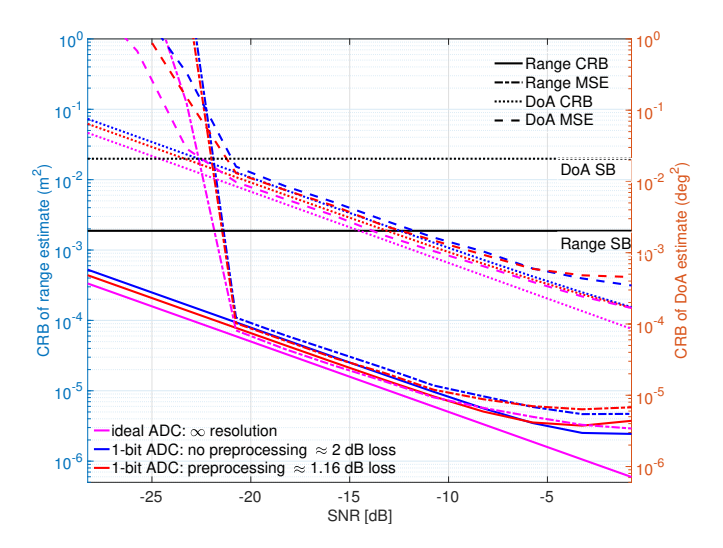


Fig. 11: Range and DoA MSE results for a target located at 30 m and  $\theta_1 = 0^{\circ}$  as a function of varying SNR. Also shown are the respective CRBs and sampling bounds based on grid spacing. It can be observed that improvements similar to the CRB are achieved in the MSE by the correlation based estimator as a result of the proposed preprocessing structure. Best viewed in color.

We refer the reader to [1], [30] for more details. Prior work [1, Ch. 7] has shown that the parabola based estimator achieves the CRB with conservative oversampling for a considerable range of SNR. We extend this technique to two dimensions and obtain the coarse range and DoA estimates

$$\hat{\ell}_{0}, \hat{\theta} = \underset{\ell_{0}, \theta}{\operatorname{argmax}} \left[ \left| \sum_{n=1}^{N_{RX}} \sum_{\ell \in \mathcal{T}} \mathbf{Y}_{ln} s^{*} [\ell - \ell_{0}] \mathbf{a}(\theta)[n] \right| \right], \quad (49)$$

where  $\mathbf{Y} \in \mathcal{C}^{|\mathcal{T}| \times N_{\text{RX}}}$  is the two dimensional time-antenna data matrix captured at the RX and  $\theta \in \Theta$ .  $\Theta$  denotes a grid of DoAs with a grid spacing of  $\delta_{DoA}$ . The coarse estimates are then refined by the parabola fitting method in range and DoA dimensions separately. For our simulations, we used  $4\times$ interpolation and  $\delta_{DoA} = 0.5^{\circ}$ . Extension to multiple targets is straightforward and involves replacing the argmax operation in (49) by a target detection procedure based on constant false alarm rate (CFAR) detection [29]. The coarse range and DoA estimates for all targets can then be individually refined by parabolic interpolation in the range and DoA dimensions. An important point here is that the correlation-based estimator is the MLE under the AWGN assumption. As discussed before, the preprocessor makes the noise correlated across antennas. We whiten the signal using  $\mathbf{R}_{\mathbf{n'n'}}^{-1}$  for the preprocessed case. We also point out here that the correlation in (49) can be implemented efficiently through FFTs. The pseudocode of the proposed procedure is given in Algorithm 1.

The MSE in range and DoA estimates resulting from Algorithm 1 for a target located at 30 m and  $\theta_1=0^\circ$  are illustrated in Fig. 11 against the RX SNR for the three ADC cases considered throughout this paper. The RX SNR is varied by changing the transmit power  $P_t$  from 10dBm to 37.5dBm.

The range and DoA CRB as well as the crude grid spacing based error bounds (The DoA sampling bound is given by  $\frac{\delta_{\rm DoA}^2}{12}$ ) are also plotted in Fig. 11. Improvements similar to the ones in range and DoA CRB are seen in the MSE for the range and DoA estimates as a result of the proposed preprocessor. All the MSE curves follow their respective CRBs before flooring at high SNR and diverging at low SNRs. The flooring at high SNRs occurs due to limited grid resolution and bias from the parabola model assumed for upsampling the correlation statistics [30]. Similar observations have been made for correlation-based estimators before [1, Ch. 7]. The results demonstrated in Fig. 11 establish that the gains observed in the range and DoA CRBs derived and computed numerically are also achievable in terms of the MSE.

## VIII. CONCLUSION

In this paper, we characterized the performance of a fully digital architecture with 1-bit ADCs in terms of CRB of parameters of interest for a radar operating in the mmWave band. We proposed an analog preprocessing structure that can be designed and optimized beforehand depending on the particular application. We demonstrated that the preprocessing network can in fact be realized through low-resolution phaseshifters. We showed that the gap between the CRB of a system with 1-bit ADCs and the CRB of a system with ideal  $\infty$  resolution ADCs can be reduced to 1.16dB using the proposed analog preprocessing unit, which is an improvement over the previously known 2db loss. We also demonstrated the achievability of the improved CRB through a simple range-DoA estimator. We showed by numerical evaluation of the CRB that this is a viable solution for future highresolution low-cost low-power sensing requirements. Future work in this direction includes the generalization of the analog preprocessing structure to an arbitrary number of RF chains, optimization of oversampling rate and algorithmic design for the use of the proposed architecture in various settings.

# APPENDIX A DERIVATIVE COMPUTATION IN (30)

This appendix details the computation of the derivatives required for (30). The derivatives  $\frac{\partial \mu_{\mathbf{y}}(\psi)}{\partial \psi_i}$  for  $\psi_i \in \{|\gamma_i|, \angle \gamma_i, \theta_i, \tau_i\}$  where  $0 \leq i \leq K$  at time  $nT_s$  are given by

$$\frac{\partial \boldsymbol{\mu}_{\mathbf{y}}(\boldsymbol{\psi})}{\partial |\gamma_{i}|} \bigg|_{t=nT_{s}} = \frac{\partial \sum_{k=0}^{K} \gamma_{k} \mathbf{a}(\theta_{k}) x (nT_{s} - \tau_{k})}{\partial |\gamma_{i}|}$$

$$= e^{\mathbf{j} \angle \gamma_{i}} \mathbf{a}(\theta_{i}) x (nT_{s} - \tau_{i}),$$
(50)

$$\left. \frac{\partial \boldsymbol{\mu}_{\mathbf{y}}(\boldsymbol{\psi})}{\partial \angle \gamma_i} \right|_{t=nT_s} = \mathbf{j} \gamma_i \mathbf{a}(\theta_i) x (nT_s - \tau_i), \tag{51}$$

$$\left. \frac{\partial \boldsymbol{\mu}_{\mathbf{y}}(\boldsymbol{\psi})}{\partial \theta_i} \right|_{t=nT_s} = \gamma_i \left( \mathbf{a}(\theta_i) \odot \mathbf{b}(\theta_i) \right) x(nT_s - \tau_i), \quad (52)$$

where

$$\mathbf{b}(\cdot) = \left[ 0 \ \frac{\mathbf{j}2\pi d \, \cos(\cdot)}{\lambda} \dots \frac{\mathbf{j}(N-1)2\pi d \, \cos(\cdot)}{\lambda} \right]^{\mathrm{T}}, \quad (53)$$

and finally

$$\frac{\partial \boldsymbol{\mu}_{\mathbf{y}}(\boldsymbol{\psi})}{\partial \tau_{i}} \bigg|_{t=nT_{s}} = \gamma_{i} \mathbf{a}(\theta_{i}) x' (nT_{s} - \tau_{i})$$

$$= \gamma_{i} \mathbf{a}(\theta_{i}) \sum_{\ell=1}^{L} s[\ell] g' (nT_{s} - \ell T_{s}), \tag{54}$$

where

$$g'(t) = \begin{cases} 0, & \text{if } t = 0\\ \frac{(\pi B)^2 t \cos(\pi B t) - \pi B \sin(\pi B t)}{(\pi B t)^2}, & \text{otherwise.} \end{cases}$$
(55)

The derivatives,  $\frac{\partial \mathrm{Re}[\mathbf{s}_k(\psi)]}{\partial \psi_i}$  and  $\frac{\partial \mathrm{Im}[\mathbf{s}_k(\psi)]}{\partial \psi_i}$ , required for the computation of (16) and (17) are given by the real and imaginary parts of the  $k^{th}$  component of (50), (51), (52) and (54) for corresponding  $\psi_i$  and  $\psi_j$ .

# $\begin{array}{c} \text{Appendix B} \\ \text{Derivative of $\mathbf{R}_{PP}$ w.r.t } \left| \alpha \right| \end{array}$

The matrix  $\mathbf{R}_{PP}$  accounts for the only difference between  $\mathbf{F}_{\text{1-bit-PP}}$  in (44) and  $\mathbf{F}_{\text{1-bit}}$  in (45). The derivative of  $\mathbf{R}_{PP}$  w.r.t  $|\alpha|$ ,  $\mathbf{R}'_{PP}$ , is given by

$$\begin{split} \mathbf{R}'_{PP} &= \frac{\partial \mathbf{R}_{PP}}{\partial |\alpha|} \\ &= \frac{1}{1 + |\alpha|^2} \bigg( -2|\alpha| \mathrm{diag}((\overline{\mathbf{A}_1})^*) (\mathrm{diag}(\overline{\mathbf{R}_{\mathbf{rr}-1}}))^{-1} \mathrm{diag}(\overline{\mathbf{A}_1}) \\ &+ \mathrm{diag}((\overline{\mathbf{A}_1})^*) (\mathrm{diag}(\overline{\mathbf{R}_{\mathbf{rr}-1}}))^{-1} \mathrm{diag}(\mathbf{F}_{N_{RX}} \mathbf{a}'_1) \\ &+ \mathrm{diag}((\mathbf{F}_{N_{RX}} \mathbf{a}'_1)^*) (\mathrm{diag}(\overline{\mathbf{R}_{\mathbf{rr}-1}}))^{-1} \mathrm{diag}(\overline{\mathbf{A}_1}) \\ &- \mathrm{diag}((\overline{\mathbf{A}_1})^*) (\mathrm{diag}(\overline{\mathbf{R}_{\mathbf{rr}-1}}))^{-2} \mathrm{diag}(\mathbf{F}_{N_{RX}} \mathbf{R}'_{\mathbf{rr}-1}) \mathrm{diag}(\overline{\mathbf{A}_1}) \bigg), \end{split}$$

where  $\mathbf{a}'_1 \in \mathcal{C}^{N_{\text{RX}}}$  is the derivative of the first row of  $\mathbf{A}$  w.r.t  $|\alpha|$  given by

$$\mathbf{a}_1' = \left[0, e^{j \angle \alpha}, 0, \dots 0\right]^T, \tag{57}$$

and  $\mathbf{R'_{rr-1}} \in \mathcal{C}^{N_{RX}}$  is the derivative of the first row of  $\mathbf{R_{rr}}$  w.r.t  $|\alpha|$  given by

$$\mathbf{R}'_{\mathbf{rr}-1} = \left[0, \frac{\partial f(\bar{\alpha})}{\partial |\alpha|}, 0, \dots \left(\frac{\partial f(\bar{\alpha})}{\partial |\alpha|}\right)^*\right]^T, \tag{58}$$

with

$$\frac{\partial f(\bar{\alpha})}{\partial |\alpha|} = \frac{2}{\pi} \left( \sqrt[-1/2]{1 - \left(\frac{\operatorname{Re}\left[\alpha\right]}{1 + |\alpha|^{2}}\right)^{2}} \times \frac{\cos(\angle \alpha)(1 + |\alpha|^{2}) - 2\operatorname{Re}\left[\alpha\right]|\alpha|}{\left(1 + |\alpha|^{2}\right)^{2}} + j \times \frac{\left(1 + |\alpha|^{2}\right)^{2}}{1 - \left(\frac{\operatorname{Im}\left[\alpha\right]}{1 + |\alpha|^{2}}\right)^{2}} \frac{\sin(\angle \alpha)(1 + |\alpha|^{2}) - 2\operatorname{Im}\left[\alpha\right]|\alpha|}{\left(1 + |\alpha|^{2}\right)^{2}} \right).$$
(59)

# $\begin{array}{c} \text{Appendix C} \\ \text{Derivative of $\mathbf{R}_{PP}$ w.r.t $\angle \alpha$} \end{array}$

The derivative of  $\mathbf{R}_{PP}$  w.r.t  $\angle \alpha$ ,  $\mathbf{R}''_{PP}$ , is given by

(54) 
$$\mathbf{R}_{PP}'' = \frac{\partial \mathbf{R}_{PP}}{\partial \angle \alpha}$$

$$= \frac{1}{1 + |\alpha|^2} \left( \operatorname{diag}((\overline{\mathbf{A}}_1)^*) (\operatorname{diag}(\overline{\mathbf{R}}_{\mathbf{rr}-1}))^{-1} \operatorname{diag}(\mathbf{F}_{N_{RX}} \mathbf{a}_1') + \operatorname{diag}((\mathbf{F}_{N_{RX}} \mathbf{a}_1')^*) (\operatorname{diag}(\overline{\mathbf{R}}_{\mathbf{rr}-1}))^{-1} \operatorname{diag}(\overline{\mathbf{A}}_1) - \operatorname{diag}((\overline{\mathbf{A}}_1)^*) (\operatorname{diag}(\overline{\mathbf{R}}_{\mathbf{rr}-1}))^{-2} \operatorname{diag}(\mathbf{F}_{N_{RX}} \mathbf{R}_{\mathbf{rr}-1}') \operatorname{diag}(\overline{\mathbf{A}}_1) \right),$$
(55) 
$$(50)$$

where  $\mathbf{a}'_1 \in \mathcal{C}^{N_{\text{RX}}}$  is the derivative of the first row of  $\mathbf{A}$  w.r.t  $\angle \alpha$  given by

$$\mathbf{a}_1' = \begin{bmatrix} 0, \mathbf{j}\alpha, 0, \dots 0 \end{bmatrix}^T, \tag{61}$$

and  $\mathbf{R'_{rr-1}} \in \mathcal{C}^{N_{RX}}$  is the derivative of the first row of  $\mathbf{R_{rr}}$  w.r.t  $\angle \alpha$  given by

$$\mathbf{R}'_{\mathbf{rr}-1} = \left[0, \frac{\partial f(\bar{\alpha})}{\partial \angle \alpha}, 0, \dots \left(\frac{\partial f(\bar{\alpha})}{\partial \angle \alpha}\right)^*\right]^T, \tag{62}$$

with

$$\frac{\partial f(\bar{\alpha})}{\partial \angle \alpha} = \frac{2}{\pi} \left( \sqrt[-1/2]{1 - \left(\frac{\operatorname{Re}\left[\alpha\right]}{1 + |\alpha|^2}\right)^2} \times \frac{-\operatorname{Im}\left[\alpha\right]}{\left(1 + |\alpha|^2\right)} + j \times \sqrt[-1/2]{1 - \left(\frac{\operatorname{Im}\left[\alpha\right]}{1 + |\alpha|^2}\right)^2} \times \frac{\operatorname{Re}\left[\alpha\right]}{\left(1 + |\alpha|^2\right)} \right).$$
(63)

# APPENDIX D PROOF OF CLAIM 1

Here we give an approximate proof of the claim made in section VI-B. An alternative way to look at the optimization of the preprocessor w.r.t  $\angle \alpha$  is to derive the stationary points of  $(\mathbf{R}_{PP})_{kk}$  in (46) w.r.t k and then evaluate (46) at these stationary points to see which k maximizes the FIM. Each k has a one-to-one correspondence with an *on-grid* DoA as detailed in section V. Before deriving the stationary points of  $(\mathbf{R}_{PP})_{kk}$  w.r.t k, we note that the expression in (46) can be simplified as

$$(\mathbf{R}_{PP})_{kk} = \frac{\left(1 + |\alpha|^2\right)^{-1} \left(1 + |\alpha|^2 + 2|\alpha|\cos\left(\frac{2\pi k}{N_{RX}} + \angle\alpha\right)\right)}{1 + 2f(\operatorname{Re}\left[\bar{\alpha}\right])\cos\left(\frac{2\pi k}{N_{RX}}\right) - 2f(\operatorname{Im}\left[\bar{\alpha}\right])\sin\frac{2\pi k}{N_{RX}}}.$$
(64)

At this point, we make an approximation by exploiting that  $asin(\cdot) \approx (\cdot)$  for small  $(\cdot)$ . It can be verified that the maximum values of Re  $[\bar{\alpha}]$  and Im  $[\bar{\alpha}]$  equal 0.5. Fig. 12 plots the percentage error resulting from the approximation  $asin(\cdot) \approx (\cdot)$  for  $|(\cdot)| \leq 0.5$  in red. It also illustrates the percentage error in phase as a function of  $\angle \alpha$  resulting from this approximation for  $|\alpha| = 1$ . It can be observed that both these errors are under 5% in the range of interest, thus justifying its use. With the approximation  $asin(\cdot) \approx (\cdot)$ , (64) can be approximated as

$$(\mathbf{R}_{PP})_{kk} \approx \frac{1 + |\alpha|^2 + 2|\alpha|\cos\left(\frac{2\pi k}{N_{RX}} + \angle\alpha\right)}{1 + |\alpha|^2 + \frac{4}{\pi}|\alpha|\cos\left(\frac{2\pi k}{N_{RY}} + \angle\alpha\right)}.$$
 (65)

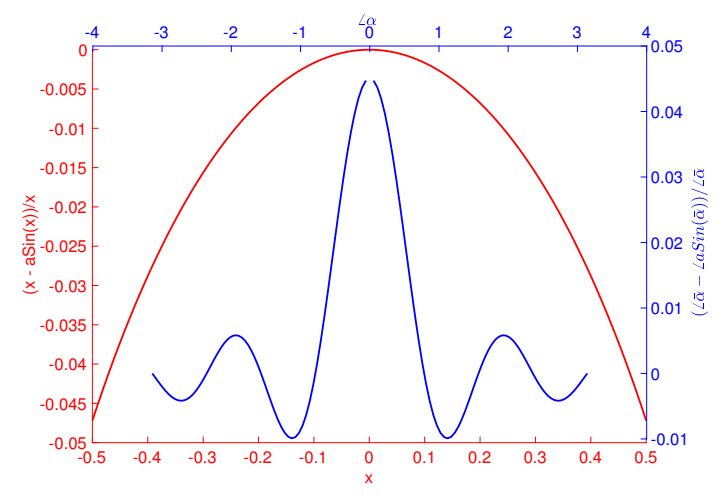


Fig. 12: Percentage error of the approx  $asin(\cdot) \approx (\cdot)$  for  $|(\cdot)| \leq 0.5$  shown in red. The blue curve plots the percentage error in phase as a function of  $\angle \alpha$  resulting from the  $asin(\cdot) \approx (\cdot)$  approximation for  $|\alpha| = 1$ . It can be seen that the error stays under 5% thus justifying the approximation. Best viewed in color.

Taking the derivative of (65) w.r.t k and equating it to 0 results in (after some algebra)

$$2|\alpha|\sin\left(\frac{2\pi k}{N_{\text{RX}}} + \angle\alpha\right) = \frac{4}{\pi}|\alpha|\sin\left(\frac{2\pi k}{N_{\text{RX}}} + \angle\alpha\right).$$
 (66)

Any k that satisfies (66) is a stationary point of (46). For  $\alpha \neq 0$ , the two sides of (66) are equal only when the argument of the  $\sin()$  is a multiple of  $\pi$ . Relaxing  $k/N_{\rm RX}$  to any real number and considering the fundamental period of the argument of  $\sin()$ , i.e.  $0 \leq \left(\frac{2\pi k}{N_{\rm RX}} + \angle \alpha\right) < 2\pi$ , this results in two stationary points  $\frac{2\pi k}{N_{\rm RX}} = -\angle \alpha$  and  $\frac{2\pi k}{N_{\rm RX}} = \pi - \angle \alpha$ . Putting these back into (65) or (46) immediately reveals that  $\frac{2\pi k}{N_{\rm RX}} = -\angle \alpha$  maximizes it. Particularly for  $|\alpha| = 1$ , putting back  $\frac{2\pi k}{N_{\rm RX}} = \pi - \angle \alpha$  into (65) yields 0 whereas  $\frac{2\pi k}{N_{\rm RX}} = -\angle \alpha$  results in 1.22 which agrees with the peak improvement over the unprocessed case as illustrated in Section VI-C.

The maximizing value of k can be mapped back to the spatial DoA using the mapping given in remark 2 of Section V resulting in  $\bar{\theta} = \sin^{-1}\left(-\frac{\lambda \angle \alpha}{2\pi d}\right)$ . This value (perhaps not surprisingly) turns out to be the same as the beamforming angle of the  $\begin{bmatrix} 1 & \alpha \end{bmatrix}$  filter (for  $|\alpha| = 1$ ) as discussed in Section IV. This concludes the proof that the preprocessing architecture achieves its maximum improvement in the beamformed direction determined by  $\angle \alpha$ .

Note: The set of values  $k/N_{\rm RX}$  is not dense in  $\mathcal R$  unless  $N_{\rm RX} \to \infty$ . Consequently, the maximum improvement in FIM, especially in the finite aperture case, does not always occur in the beamforming angle of the  $[1 \quad \alpha]$  filter. Instead, the maximum improvement at one of the neighboring on-grid angles corresponding to the array aperture. The approximation  $\mathrm{asin}(\cdot) \approx (\cdot)$  also adds a little bias to the results obtained using the above analysis.

#### ACKNOWLEDGMENT

This work was supported by a gift from Qualcomm Inc.

#### REFERENCES

- [1] M. A. Richards, "Fundamentals of radar signal processing," pp. 41–106. Tata McGraw-Hill Education, 2005.
- [2] R. W. Heath Jr., N. Gonzlez-Prelcic, S. Rangan, W. Roh, and A. M. Sayeed, "An overview of signal processing techniques for millimeter wave MIMO systems," *IEEE Journal of Selected Topics in Signal Processing*, vol. 10, no. 3, pp. 436–453, April 2016.
- [3] J. Li, M. M. Naghsh, S. J. Zahabi, and M. Modarres-Hashemi, "Compressive radar sensing via one-bit sampling with time-varying thresholds," in *Proc. of 50th Asilomar Conference on Signals, Systems and Computers*, Nov 2016, pp. 1164–1168.
- [4] S. J. Zahabi, M. M. Naghsh, M. Modarres-Hashemi, and J. Li, "Compressive pulse-doppler radar sensing via 1-bit sampling with time-varying threshold," in *Proc. of IEEE International Conference on Acoustics, Speech and Signal Process. (ICASSP)*, March 2017, pp. 3419–3423.
- [5] X. Dong and Y. Zhang, "A MAP approach for 1-bit compressive sensing in synthetic aperture radar imaging," *IEEE Geoscience and Remote Sensing Letters*, vol. 12, no. 6, pp. 1237–1241, June 2015.
- [6] F. Xi and S. Chen, "Super-resolution pulse-doppler radar sensing via one-bit sampling," in *Proc. of IEEE 10th Sensor Array and Multichannel* Signal Process. Workshop (SAM), July 2018, pp. 232–236.
- [7] A. Mezghani, F. Antreich, and J. A. Nossek, "Multiple parameter estimation with quantized channel output," in *Proc. of 2010 International ITG Workshop on Smart Antennas (WSA)*, Feb 2010, pp. 143–150.
- [8] T. Koch and A. Lapidoth, "At low SNR, asymmetric quantizers are better," *IEEE Trans. on Inf. Theory*, vol. 59, no. 9, pp. 5421–5445, Sept 2013.
- [9] T. Koch and A. Lapidoth, "Increased capacity per unit-cost by oversampling," in *Proc. of IEEE 26th Convention of Electrical and Electronics Engineers in Israel*, Nov 2010, pp. 000684–000688.
- [10] A. Mezghani and J. A Nossek, "Capacity lower bound of MIMO channels with output quantization and correlated noise," in *Proc. of IEEE International Symposium on Information Theory Proceedings (ISIT)*, 2012.
- [11] M. Schluter, M. Dorpinghaus, and G. P. Fettweis, "Bounds on channel parameter estimation with 1-bit quantization and oversampling," in Proc. of 2018 IEEE 19th International Workshop on Signal Processing Advances in Wireless Communications (SPAWC), June 2018, pp. 1–5.
- [12] S. Rao, A. Mezghani, and A. L. Swindlehurst, "Channel estimation in one-bit massive MIMO systems: Angular versus unstructured models," *IEEE Journal of Selected Topics in Signal Processing*, vol. 13, no. 5, pp. 1017–1031, Sep. 2019.
- [13] F. Wendler, M. S. Stein, A. Mezghani, and J. Nossek, "Quantization-loss reduction for 1-bit boc positioning," in *Proc. of 2013 International Technical Meeting of The Institute of Navigation*, March 2013, pp. 509–518.
- [14] M. S. Stein, "Performance analysis for time-of-arrival estimation with oversampled low-complexity 1-bit A/D conversion," in *Proc. of* 2017 IEEE International Conference on Acoustics, Speech and Signal Processing (ICASSP), March 2017, pp. 4491–4495.
- [15] M. Stein, F. Wendler, A. Mezghani, and J. A. Nossek, "Quantization-loss reduction for signal parameter estimation," in *Proc. of 2013 IEEE International Conference on Acoustics, Speech and Signal Processing*, May 2013, pp. 5800–5804.
- [16] J. J. Bussgang, "Crosscorrelation functions of amplitude-distorted gaussian signals," in *Technical Report No. 216, MIT, Cambridge, MA*, March 1952.
- [17] M. Stein, A. Mezghani, and J. A. Nossek, "A lower bound for the Fisher information measure," *IEEE Signal Process. Letters*, vol. 21, no. 7, pp. 796–799, July 2014.
- [18] P. Kumari, K. U. Mazher, A. Mezghani, and R. W. Heath Jr., "Low resolution sampling for joint millimeter-wave MIMO communicationradar," in *Proc. of IEEE Statistical Signal Process. Workshop (SSP)*, June 2018, pp. 193–197.
- [19] P. Kumari, J. Choi, N. Gonzlez-Prelcic, and R. W. Heath Jr., "IEEE 802.11ad-based radar: An approach to joint vehicular communicationradar system," *IEEE Trans. on Veh.Technol.*, vol. 67, no. 4, pp. 3012– 3027, April 2018.

- [20] K. U. Mazher, A. Mezghani, and R. W. Heath Jr., "Low resolution millimeter wave radar: Bounds and performance," in *Proc. of 2018* 52nd Asilomar Conference on Signals, Systems, and Computers, Oct 2018, pp. 554–558.
- [21] J. Li and P. Stoica, "MIMO radar with colocated antennas," *IEEE Signal Processing Magazine*, vol. 24, no. 5, pp. 106–114, Sep. 2007.
- [22] S. M. Patole, M. Torlak, D. Wang, and M. Ali, "Automotive radars: A review of signal processing techniques," *IEEE Signal Processing Magazine*, vol. 34, no. 2, pp. 22–35, March 2017.
- [23] J. Hasch, E. Topak, R. Schnabel, T. Zwick, R. Weigel, and C. Wald-schmidt, "Millimeter-wave technology for automotive radar sensors in the 77 GHz frequency band," *IEEE Trans. on Microwave Theory and Techniques*, vol. 60, no. 3, pp. 845–860, March 2012.
- [24] S. M. Kay, "Cramer-Rao lower bound," in Fundamentals of statistical signal processing: Estimation theory, pp. 27–82. Prentice Hall Inc., 1993
- [25] R. Zamir, "A proof of the Fisher information inequality via a data processing argument," *IEEE Trans. on Information Theory*, vol. 44, no. 3, pp. 1246–1250, May 1998.
- [26] R. M. Gray, "Circulant matrices," in *Toeplitz and circulant matrices: A review*, pp. 31–36. Now Publishers., 2006.
- [27] R. Mendez-Rial, C. Rusu, A. Alkhateeb, N. Gonzlez-Prelcic, and R. W. Heath, "Channel estimation and hybrid combining for mmWave: Phase shifters or switches?," in *Proc. of 2015 Information Theory and Applications Workshop (ITA)*, Feb 2015, pp. 90–97.
- [28] M. Lu, K. Wevers, and R. V. D. Heijden, "Technical feasibility of advanced driver assistance systems (ADAS) for road traffic safety," *Transportation Planning and Technology*, vol. 28, no. 3, pp. 167–187, 2005
- [29] H. Rohling, "Ordered statistic CFAR technique an overview," in 2011 12th International Radar Symposium (IRS), Sep. 2011, pp. 631–638.
- [30] G. Jacovitti and G. Scarano, "Discrete time techniques for time delay estimation," *IEEE Trans. on Signal Processing*, vol. 41, no. 2, pp. 525– 533, Feb 1993.



ROBERT W. HEATH JR. (Fellow, IEEE) received the B.S. and M.S. degrees from the University of Virginia, Charlottesville, VA, in 1996 and 1997, respectively, and the Ph.D. degree from Stanford University, Stanford, CA, in 2002, all in electrical engineering. From 1998 to 2001, he was a Senior Member of the Technical Staff then a Senior Consultant with Iospan Wireless, Inc., San Jose, CA, where he worked on the design and implementation of the physical and link layers of the first commercial MIMO-OFDM communication system.

From 2002?2020, he was with The University of Texas at Austin, most recently as Cockrell Family Regents Chair in Engineering and Director of UT SAVES. He is presently a Distinguished Professor with North Carolina State University. He is also President and CEO of MIMO Wireless Inc. He authored Introduction to Wireless Digital Communication (Prentice Hall, 2017) and Digital Wireless Communication: Physical Layer Exploration Lab Using the NI USRP (National Technology and Science Press, 2012), and coauthored Millimeter Wave Wireless Communications (Prentice Hall, 2014) and Foundations of MIMO Communication (Cambridge University Press, 2018). He is currently Editor-in-Chief of IEEE Signal Processing Magazine and is a member-at-large of the IEEE Communications Society Board of Governors.

Dr. Heath has been a coauthor of a number award winning conference and journal papers including recently the 2016 IEEE Communications Society Fred W. Ellersick Prize, the 2016 IEEE Communications and Information Theory Societies Joint Paper Award, the 2017 Marconi Prize Paper Award, and the 2019 IEEE Communications Society Stephen O. Rice Prize. He was the recipient of the 2017 EURASIP Technical Achievement award and the 2019 IEEE Kiyo Tomiyasu Award. He was a Distinguished Lecturer and member of the Board of Governors in the IEEE Signal Processing Society. In 2017, he was selected as a Fellow of the National Academy of Inventors. He is also a licensed Amateur Radio Operator, a Private Pilot, a registered Professional Engineer in Texas.



KHURRAM USMAN MAZHER received his B.S. degree in electrical engineering from Lahore University of Management Sciences in 2015 and M.S. degree in electrical engineering from The University of Texas at Austin in 2019. He is now a PhD student at The University of Texas at Austin. He was awarded the Qualcomm Innovation Fellowship in 2020. His research interests include the application of signal processing and machine learning to wireless communications, radar signal processing and positioning systems.



AMINE MEZGHANI (Member, IEEE) received the Ph.D. degree in electrical engineering from the Technical University of Munich, Germany in 2015. He is currently an Assistant Professor with the Department of Electrical and Computer Engineering, the University of Manitoba, Canada. Prior to this, he was a Postdoctoral Fellow with the University of Texas at Austin, the USA, and a Postdoctoral Scholar with the Department of Electrical Engineering and Computer Science, University of California, Irvine, USA. He has authored or coauthored about a hun-

dred papers, particularly on the topic of signal processing and communications with low-resolution analog-to-digital and digital-to-analog converters. His current research interests include millimeter-wave communications, massive MIMO, hardware constrained radar and communication systems, antenna theory, and large-scale signal processing algorithms. He was the recipient of the joint Rohde & Schwarz and EE department Outstanding Dissertation Award in 2016.